MASTERARBEIT / MASTER’S THESIS

Titel der Masterarbeit / Title of the Master’s Thesis

„Predicting the limits of the ELT: An exercise in tempering expectations for studies of the initial mass function with the ELT in the galactic centre and beyond“

verfasst von / submitted by

Alarich Herzner BSc.

angestrebter akademischer Grad / in partial fulfilment of the requirements for the degree of

Master of Science (MSc)

Wien, 2022 / Vienna, 2022

Studienkennzahl lt. Studienblatt / degree programme code as it appears on the student record sheet:	UA 066 910
Studienrichtung lt. Studienblatt / degree programme as it appears on the student record sheet:	Masterstudium Computational Science UG2002
Betreut von / Supervisor:	Univ.-Prof. Joao Alves, PhD
Mitbetreut von / Co-Supervisor:	Dr. Kieran Leschinski, MSc

Abstract

With its completion planned for 2027, the Extremely Large Telescope (ELT) may be used for studies of the Initial Mass Function (IMF) near the Galactic Centre. Detailed knowledge of the full IMF in environments significantly different to the solar neighbourhood is paramount to enabling astronomers to better understand the formation and evolution of galaxies from the Big-Bang right up to the present day.

The aim of this master thesis is to find the lowest mass limits for reliably determining whether or not a star belongs to a star cluster in different galactic environments. In particular this work aims to find where the reliability limit will be for future IMF studies in the galactic centre when using the ELT. The results of this work will help to set expectations in the IMF community about which open questions may realistically be answered with the next generation of extremely large telescopes.

To achieve this goal a piece of software has been developed which is able to simulate realistic distributions of stars in any area of the Milky Way. Using the software, mock observations with differing cluster masses and locations from the galactic anti centre to the galactic centre have been simulated. The resulting data has been converted into sets of observational images representing multi-epoch observations with MICADO at the ELT. Star positions and flux has been extracted from the images with photometric techniques provided by `photutils`. From these time stamped positions the proper motion has been estimated, since the position alone is not enough information to determine if a given star is a field star or a member of a cluster. Cluster analysis was performed on proper motion in conjunction with positions and apparent magnitude.

Finally, the performance of the analysis was measured leveraging the ground truth set (the simulated cluster and field stars). These performance measures were evaluated for different stellar mass ranges (low-, solar-, high-mass stars) in order to determine the reliability and completeness of cluster memberships within a given mass range. Hence, indicating in which ranges the IMF studies will be possible.

According to our results, the cluster membership for low mass ($<1 \times 10^4\,\mathrm{M}_\odot$) clusters can be reliably determined for masses $>0.5\,\mathrm{M}_\odot$ in the galactic centre, but expected to be acceptable in all studied mass regimes including $0.5\,\mathrm{M}_\odot$ to $0.08\,\mathrm{M}_\odot$ for truly massive (e.g. $>1 \times 10^4\,\mathrm{M}_\odot$) clusters. Outside of the Galactic Centre (GC), the full IMF is available in all simulated young star clusters out to $8\,\mathrm{kpc}$.

Kurzfassung

Das Extremely Large Telescope (ELT), dessen Fertigstellung für 2027 geplant ist, kann für Untersuchungen der ursprünglichen Massenfunktion, auf Englisch Initial Mass Function (IMF), in der Nähe des galaktischen Zentrums eingesetzt werden. Detaillierte Kenntnisse der gesamten IMF in Umgebungen, die sich deutlich von der Sonnenumgebung unterscheiden, sind von entscheidender Bedeutung, um den Astronomen ein besseres Verständnis der Entstehung und Entwicklung von Galaxien vom Urknall bis heute zu ermöglichen.

Ziel dieser Masterarbeit ist es, die untersten Massengrenzen für die zuverlässige Bestimmung der Zugehörigkeit eines Sterns zu einem Sternhaufen in verschiedenen galaktischen Umgebungen zu finden. Insbesondere soll mit dieser Arbeit herausgefunden werden, wo die Zuverlässigkeitsgrenze für zukünftige IMF-Studien im galaktischen Zentrum liegt, wenn das ELT verwendet wird. Die Ergebnisse dieser Arbeit werden dazu beitragen, in der IMF-Gemeinschaft Erwartungen darüber zu setzen, welche offenen Fragen mit der nächsten Generation von extrem großen Teleskopen realistisch beantwortet werden können.

Um dieses Ziel zu erreichen, wurde eine Software entwickelt, die in der Lage ist, realistische Verteilungen von Sternen in einem beliebigen Gebiet der Milchstraße zu simulieren. Mit Hilfe der Software wurden Beobachtungen mit unterschiedlichen Sternhaufenmassen und Positionen vom galaktischen Antizentrum bis zum galaktischen Zentrum simuliert. Die daraus resultierenden Daten wurden in Sätze von Beobachtungsbildern umgewandelt, die Multi-Epochen-Beobachtungen mit MICADO am ELT darstellen. Sternpositionen und Lichtstrom wurden aus den Bildern mit photometrischen Techniken extrahiert, die von `photutils` bereitgestellt wurden. Aus diesen zeitgestempelten Positionen wurde die Eigenbewegung geschätzt, da die Position allein nicht ausreicht, um zu bestimmen, ob ein bestimmter Stern ein Feldstern oder ein Mitglied eines Haufens ist. Die Clusteranalyse wurde anhand der Eigenbewegung in Verbindung mit den Positionen und der scheinbaren Helligkeit durchgeführt.

Schließlich wurde die Leistung der Analyse mit Hilfe der Kenntnis über die korrekte Zuordnung (simulierter Sternhaufen und Feldsterne) bestimmt. Diese Leistungsbestimmungen wurden für verschiedene Sternmassenbereiche (Sterne mit niedriger, solarer und hoher Masse) ausgewertet, um die Zuverlässigkeit und Vollständigkeit der Haufenmitgliedschaften innerhalb eines bestimmten Massenbereichs zu bestimmen. Somit kann angegeben werden, in welchen Bereichen die IMF-Studien möglich sind.

Nach unseren Ergebnissen kann die Cluster-Zugehörigkeit für massearme ($<1\times10^4\,\mathrm{M}_\odot$) Sternhaufen für Massen $>0.5\,\mathrm{M}_\odot$ im galaktischen Zentrum zuverlässig bestimmt werden, aber es wird erwartet, dass sie in allen untersuchten Massenbereichen einschließlich $0.5\,\mathrm{M}_\odot$ bis $0.08\,\mathrm{M}_\odot$ für wirklich massereiche ($>1\times10^4\,\mathrm{M}_\odot$) Haufen akzeptabel ist. Außerhalb des galaktischen Zentrums ist die volle IMF in allen simulierten jungen Sternhaufen bis zu $8\,\mathrm{kpc}$ verfügbar.

Acknowledgement

Many thanks to Dr. Kieran Leschinski for his many important suggestions, hints and patience along the long and winding road. I would also like to thank Prof. João Alves for the opportunity to work in his team and his perspective as an experienced astrophysicist. Finally yet importantly, many thanks to my parents Eva and Kai Mundprecht as well as my partner Viktoria Grill for their mental support and encouragement.

Contents

List of Tables

List of Figures

Chapter 1

Introduction

The ELT is currently under construction [16]. This first next generation 40m class telescope will have the resolution and sensitivity needed to study the motions of individual stars in the GC. These position and motions can be used to detect star clusters using some type of clustering algorithm and consequently estimate their Initial Mass Function (IMF). The IMF describes the mass distribution of a set of stars after the star formation process is complete, but before a star has had the opportunity to be removed from the set by ejection or burnout. The IMF is useful in many different scenarios, such as estimating the number of distant lower-mass stars by knowing the number of high-mass stars, or in understanding the star formation process itself. Whether the IMF of star clusters is universal is the subject of discussion [4] at this time. The study of Young Massive Clusters (YMCs) [50] near the GC will hopefully give more insight into this hotly debated topic. YMCs are tightly grouped clusters of stars, generally containing $>$10000 members. All original members are still present and the IMF is well sampled in all mass regimes. These facts combine to give a good picture of the end product of a star formation event. Knowing the IMF allows astronomers to better understand and model the evolution of galaxies over the whole history of the universe.

Given detected star clusters the question remains, how reliable the classification of, especially low mass, stars is. That is, which of the discovered low-mass stars actually belong to the cluster and which are field stars. If the true classification of the studied set of stars is known, the performance of the clustering algorithm and hence the reliability of the results can be calculated. However, this is generally not the case.

In this master thesis an N-body simulation containing cluster stars and field stars under the influence of the milky way potential is performed (Chapter 2). Snapshots are taken at different timesteps and fed to ScopeSim [37] to create mock observations. With the help of Photutils [11] positions and apparent magnitudes are extracted (Chapter 3). The DBSCAN algorithm used to detect cluster and field stars (Chapter 4). Finally, the reliability of the results can be determined by comparing its results with the initially simulated stars (Chapter 5).

Chapter 2

Modeling The Milky Way Galaxy

> Also lautet ein Beschluss:
> Daß der Mensch was lernen muß. -
>
> Wilhelm Busch, Max und Moritz [12]

The first mayor goal is to create and store data which will be observable by the ELT. This data consists of FSs and cluster stars at consecutive points in time. A FS is any star belonging to the milky way which is not of interest for the observation. Still, the amount, mass and velocity of these stars should be reasonably realistic. In order to study the effects of the cluster location on its observability, the model must be able to produce data for arbitrary view directions of the ELT. In a typical N-body simulation all N bodies would be simulated. However, a model containing every single star present in the MW is not a feasible option for the typical home computer. Therefore, only stars within the field of view (FOV) of the ELT are simulated. The gravitational interaction of stars inside and outside the field of view is modelled via a galactic potential. Hence, the simulated FSs do not interact at all. This simplification can not be made for cluster stars due to their proximity to each other within the cluster. Thus, cluster stars do interact with each other gravitationally. The mass of cluster and FSs are sampled from different IMFs. The positions and velocities of FSs are derived from the galactic potential. The positions and velocities of cluster stars are generated using the Plummer model, resulting in an overall stationary cluster. The circular velocity at the cluster location is derived from the galactic potential and added to each cluster star. After this initialization is complete, the simulation is run for a set amount of timesteps storing all relevant data in a database.

2.1 Required Methods

2.1.1 Sampling distribution functions

Space, velocity and mass distributions are sampled during various steps of the initialization using the following two methods. For further details and alternative methods see [17].

Rejection sampling

A proposed distribution function $g(x)$ is sampled and each resulting sample accepted with a probability of $\frac{f(x)}{Cg(x)}$. C is a constant ensuring $f(x) \leqslant Cg(x) \forall x$ and $f(x)$ the target distribution. If $g(x)$ is the probability density function (PDF) of a uniform distribution with $x \in [a, b]$

$$g(x) = \frac{1}{b-a} \tag{2.1}$$

and m the maximum of $f(x)$ within $[a, b]$ then $C = \frac{m}{b-a}$ and the acceptance criterion becomes

$$u \leq f(x) \tag{2.2}$$

here u is a uniform distribution $U(0, Cg(x)) = U(0, m)$. While $Cg(x)$ has to be larger than $f(x)$, the area between them should be as small as possible to ensure a decent acceptance fraction.

Inverse transform sampling

If the cumulative distribution function (CDF) of the probability distribution $f(y)$ is continuous and its inverse obtainable, this method can be utilized and is more efficient than rejection sampling. The CDF describes the probability that the random variable is smaller or equal to x

$$F(x) = P(X \leq x) = \int_{-\infty}^{x} f(y)dy \tag{2.3}$$

The inverse $F^{-1}(y)$ may be calculated via $F(F^{-1}(y)) = y$. With y drawn from a uniform distribution the results of $F^{-1}(y)$ have the desired probability distribution $f(y)$.

2.1.2 Integration techniques

Numerical integration is needed during initialization and simulation. Various options for time integration have been implemented. The GNU Scientific Library (GSL) [22] is used for integrations performed during initialization. The relevant functions are all based on QAG or QAGI, which have been ported from the Fortran library QUADPACK [47] to C in GSL. The decision trees given on page 79-80 in [47] help with the decision on when and how to use the respective methods.

Quadrature, Adaptive, General-purpose (QAG)

This algorithm makes use of adaptive Gauss-Kronrod quadrature to estimate the definite integral of a given function.
Quadrature sums are defined as

$$Q_n[a, b] \equiv \sum_{i}^{n} w_i f(x_i) \cong \int_{a}^{b} w(x) f(x) \mathrm{d}x \tag{2.4}$$

where w_i are weights, x_i nodes, $w(x)$ a weight function. The highest possible degree of precision is 2n-1. With this maximum precision Q_n is exact for polynomials of a degree smaller or equal to 2n-1.
Using classical Gaussian quadrature formulae, error estimation, by increasing n to n+1, requires n+1 evaluations of $f(x)$ in addition to n evaluations from calculation of the original sum, since the respective nodes have no common points. By doing so, the degree of precision is only increased from 2n-1 to 2n+1. Therefore, the error estimation obtained by subtracting the two sums could be unreliable.
Adding n+1 points to the Gauss-Legendre formula - here $w(x) = 1$ and the nodes are zeros of the Legendre polynomial - Kronrod introduced the option of increasing the precision to 3n+1, again requiring n+1 additional evaluations of $f(x)$ [44].

$$Q_n^K[a, b] \equiv \sum_{i}^{n} w_i f(x_i) + \sum_{j}^{n+1} w_j^{\cdot} f(x_j^{\cdot}) \cong \int_{-1}^{1} f(x) \mathrm{d}x \tag{2.5}$$

QAG makes use of this option, bisecting the interval with the largest local absolute error estimate in each step. This division is repeated until either the absolute or relative global error estimate is smaller than required by the caller.

Quadrature, Adaptive, General-purpose, Infinite interval (QAGI)

In case of a semi-infinite interval $(a, \pm\infty)$, the integration variable is transformed

$$x = a \pm \frac{1-t}{t} \tag{2.6}$$

leading to

$$\int_a^{\pm\infty} f(x)\mathrm{d}x = \pm \int_0^1 f\left(a \pm \frac{1-t}{t}\right) t^{-2}\mathrm{d}t \tag{2.7}$$

For an infinite interval

$$\int_{-\infty}^{\infty} f(x)\mathrm{d}x = \int_0^{\infty} f(x) + f(-x)\mathrm{d}x = \int_0^1 \left(f\left(\frac{1-t}{t}\right) + f\left(\frac{t-1}{t}\right)\right) t^{-2}\mathrm{d}t \tag{2.8}$$

After the transformation QAGS with the 15-point Kronrod rule is used. QAGS, in addition to the adaptive bisection (see QAG), makes use of the Wynn ϵ-algorithm to accelerate the convergence.

Velocity Verlet Algorithm

For cluster members the acceleration is a combination of the force resulting from the presence of all other cluster stars (see Barens Huts Algorithm) and from the milky way potential. The acceleration of FSs solely comes from the milky way potential. In each time step both velocity and acceleration of each star is evaluated.
Since the velocity, $v(t)$ changes over time, its value at the midpoint between the current (t_n) and the next timestep t_{n+1} is intuitively a better approximation than $v(t_n)$ or $v(t_{n+1})$. The same holds true for the acceleration. This leads to [21]

$$\begin{aligned} x_{n+1} &= x_n + hv_{n+0.5} \\ v_{n+1.5} &= v_{n+0.5} + \frac{h}{m}F(x_{n+1}) \end{aligned} \tag{2.9}$$

where h is the time step size $h \equiv \Delta t \equiv t_{n+1} - t_n$, F is the sum of forces equivalent to the negative gradient of the potential and x is the position.
Equation 2.9 is the Leapfrog algorithm. If one needs x and v at the same time, (2.9) can be split into two half steps.

$$\begin{aligned} v_{n+0.5} = v_n + \frac{h}{2m}F(x_n)x_{n+1} &= x_n + hv_{n+0.5} \\ v_{n+1} &= v_{n+0.5} + \frac{h}{2m}F(x_{n+1}) \end{aligned} \tag{2.10}$$

$F(x)$ does not have to be calculated twice, because $F(x_{n+1})$ can be used as $F(x_n)$ in the next timestep.

Barnes-Hut Algorithm (BH)

When determining the gravitational force acting on a star belonging to a cluster, the positions of all other stars in that cluster have to be taken into account.

$$m_i\vec{x}_i = G \sum_{j=1, j\neq i}^{N} \frac{m_i m_j \left(\vec{x}_j - \vec{x}_i\right)}{\left|\vec{x}_j - \vec{x}_i\right|^3} \tag{2.11}$$

Calculating this force for all stars requires $O(n^2)$ operations. However, the simulated clusters consist of $\sim 10^4 - 10^5$ stars. While the resulting number of calculations is possible, it is not

feasible for a typical desktop computer. Therefore, the Barnes-Hut algorithm (BH) has been implemented which is of order $O(n \log(n))$.
The gist of the BH is to approximate a set of stars by their total mass and centre of mass (COM) if the distance between them and the star, for which the force is to be calculated, is large enough. The total mass and COM of a set of N stars is

$$\begin{aligned} m_{COM} &= \sum_{i=1}^{N} m_i \\ \vec{x}_{COM} &= \frac{1}{m_{COM}} \sum_{i=1}^{N} m_i \vec{x}_i \end{aligned} \tag{2.12}$$

All cluster stars are stored in an octree. An octree is a data structure where each node in the tree has up to eight child nodes. These nodes split the space represented by their parent node into eight cubes. External nodes are nodes without any children. Each external node contains at most one star. Internal nodes have at least one child. They represent stars stored in their child nodes by storing their total mass and COM. The root node contains the whole space occupied by the cluster. Each node stores the following information: total mass, amount and center of mass of stars contained within the cube, two points defining the volume of the cube, one point at the center of the cube as well as links (pointers) to each child node and to the parent node. If a child pointer is null, it does not exist yet. The seemingly redundant point at the center of the cube is used to evaluate the child node of a star within the cube. The two points defining the volume could be used instead but that approach would require additional floating point operations.
Stars are added recursively starting at the root node. If the current node is already an internal node, the star is passed to the appropriate child. Mass and com of the internal node are updated. The appropriate child is determined by comparing the position of the star with the center of the node. If the considered node is an external node but already contains a star, both the newly added and already present star are passed down to the appropriate child or children. Consequently, the current node becomes an internal node. Since both stars can lie in the same octant, this can lead to additional recursions until the stars are assigned to different child nodes. If the current node is external and does not yet contain a star, the star is added to the node and the recursion ends.
When calculating the gravitational force on a star, the octree is travelled through recursively beginning with the root node. In case the distance d between the star and a node is sufficiently large, the stars within that node are approximated by the mass and com of that node, otherwise all child nodes within the current node are considered. Whenever the distance criterion is met, the acceleration vector stemming from the force is calculated, added to the overall acceleration of the star and the recursion for the considered branch stops.
Whether or not d is big enough, is determined by the quotient θ.

$$\theta = \frac{s}{d} < \theta_{max} \tag{2.13}$$

with s the side length of the cube and θ_{max} a set threshold value. In the special case of $\theta_{max} = 0$, BH becomes a direct-sum algorithm. $\theta_{max} = 0.5$ is a commonly chosen value.

2.2 Star clusters

A cluster can be characterised via a number of parameters, namely its density profile, metallicity, binary fraction and IMF. The following sections cover methods implemented by the author. Alternatively, cluster stars can be generated using the open source code McLuster [34] which supports more density profiles and all other parameters mentioned above. The generated file can then be imported into the database when starting a new simulation by setting the appropriate parameters. Consequently McLuster has been used for all experiments presented here.

2.2.1 Initial Mass Function

The IMF describes the initial mass distribution of stars, that is, how many stars have which mass in some set of stars at the start. It is subject of debate whether the IMF of star clusters is universal [4]. The PDMF usually differs from the IMF because massive stars burn faster an die younger. The field star PDMF represents the remnants of all star forming events that have happen over the last 10 Gyr.
Figure 13 in [19] depicts the Salpeter IMF [54] and the PDMF of Arches. Because the Arches cluster is still very young, it is fair to assume that the Arches PDMF has not changed much from its theoretical IMF. Hence it may be assumed that the IMF is an adequate estimate for the PDMF of a generic YMSC. Sampling routines for the following two IMFs have been implemented by the author.

Salpeter IMF

$$p(m) = \frac{dN}{dm} = A \cdot m^{-\alpha} \tag{2.14}$$

where p is the probability of stars having mass in range m to $m + dm$, dN is the number of stars within that range, A is a constant defining the local stellar density and α is the exponent dictating the slope of the function.
This comparatively simple and widely used ([55], [51], [25]) IMF can be sampled using inverse transform sampling. To do so one must integrate the IMF over the mass and normalize it, yielding the normalized cumulative distribution function (NCDF).

$$P(m) = \int_{m_{min}}^{m} A \cdot m^{-\alpha} dm = \frac{A}{-\alpha + 1} \left(m^{-\alpha+1} - m_{min}^{-\alpha+1} \right) \tag{2.15}$$

A is defined by normalization:

$$P(m_{max}) \equiv 1 \rightarrow A = \frac{-\alpha + 1}{m_{max}^{-\alpha+1} - m_{min}^{-\alpha+1}} \tag{2.16}$$

With this (2.15) becomes:

$$P(m) = \frac{m^{-\alpha+1} - m_{min}^{-\alpha+1}}{m_{max}^{-\alpha+1} - m_{min}^{-\alpha+1}} \tag{2.17}$$

Since Salpeter is a power-law distribution function, the inverse of the NCPF can be calculated analytically. After some simplifications the final result reads

$$m_{rand} = m_{min} \cdot \left[1 + x \cdot \left(\left(\frac{m_{max}}{m_{min}} - 1 \right)^{-\alpha+1} \right) \right]^{\frac{1}{-\alpha+1}} \tag{2.18}$$

where x is a random number in range [0,1]

Broken Power Law

The Salpeter IMF is well suited for stars above $0.5\,\mathrm{M}_{\odot}$, below this low-mass cut-off the slope of more recent IMFs [31] flatten. Broken Power Law (BPL) is used to model these functions.
The BPL IMF has the benefit of being highly adaptable. It can be utilized to approximate any IMF. It has been used to describe both globular cluster IMFs [5] as well as young star cluster IMFs ([49], [33]).

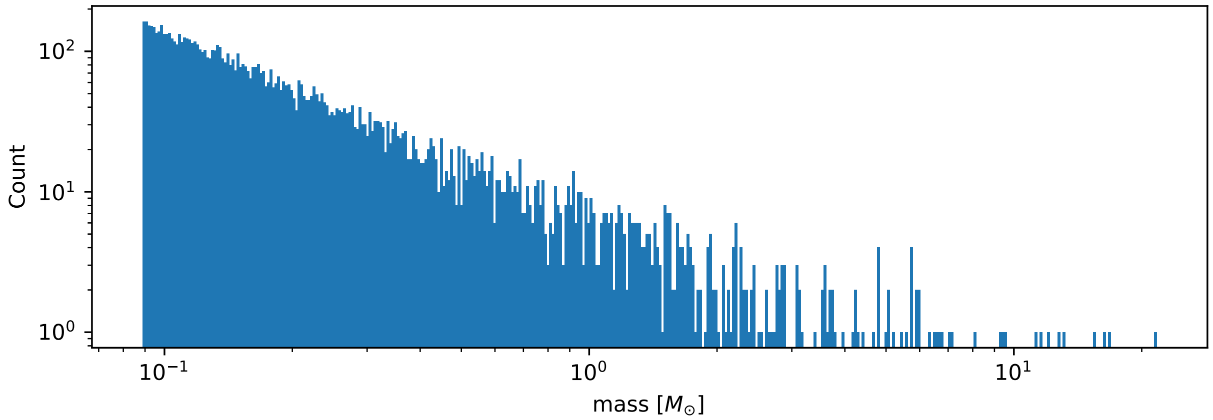

Figure 2.1: 10^3 stars sampled from the Salpeter IMF. This figure was generated to demonstrate that the author's implementation of the sampling algorithm produces realistic results.

The following is a generalization of the equation given by [32] for $n-1$ intervals.

$$\xi(m) = A \begin{cases} k_1 m^{-\alpha_1} & \text{if } m_1 \leqslant m < m_2 \\ k_2 m^{-\alpha_2} & \text{if } m_2 \leqslant m < m_3 \\ \dots & \\ k_{n-1} m^{-\alpha_{n-1}} & \text{if } m_{n-1} \leqslant m < m_n \end{cases} \tag{2.19}$$

where A is a normalization constant, $\xi(m)$ is the IMF, more intuitively $\xi(m)dm$ is the number of stars with mass between m and $m+dm$ and k_i is defined as

$$\begin{aligned} k_1 &= m_2^{\alpha_1} \\ k_2 &= m_2^{\alpha_2} \\ k_i &= k_{i-1} m_i^{\alpha_i - \alpha_{i-1}} \end{aligned} \tag{2.20}$$

As in the case of Salpeter, random samples are drawn with inverse transform sampling. The NCDF $F(m)$ can be obtained by integrating $\xi(m)$ over the mass interval.

$$F(m) = \int_{m_1}^{m} \xi(m)\, dm \tag{2.21}$$

Where A is defined by the normalization constraint:

$$A \cdot \sum_{i=1}^{n-1} \left(k_i \int_{m_i}^{m_{i+1}} m^{-\alpha_i}\, dm \right) = 1 \tag{2.22}$$

Inverting the NCDF (2.21) leads to

$$F^{-1}(y) = \begin{cases} \left[\frac{(1-\alpha_1)y}{A\cdot k_1} + m_1^{1-\alpha_1} \right]^{\frac{1}{1-\alpha_1}} \\ \text{if } 0 \leqslant y < \frac{A\cdot k_1}{1-\alpha_1} \left(m_2^{1-\alpha_1} - m_1^{1-\alpha_1} \right) \\ \left\{ \left[y - \frac{A\cdot k_1}{1-\alpha_1} \left(m_2^{1-\alpha_1} - m_1^{1-\alpha_1} \right) \right] \frac{1-\alpha_2}{A\cdot k_2} + m_2^{1-\alpha_2} \right\}^{\frac{1}{1-\alpha_2}} \\ \text{if } \frac{A\cdot k_1}{1-\alpha_1} \left(m_2^{1-\alpha_1} - m_1^{1-\alpha_1} \right) \leqslant y < \sum_{i=1}^{2} \frac{A\cdot k_i}{1-\alpha_i} \left(m_{i+1}^{1-\alpha_i} - m_i^{1-\alpha_i} \right) \\ \dots \\ \left\{ \left[\sum_{i=1}^{n-2} y - \frac{A\cdot k_i}{1-\alpha_i} \left(m_{i+1}^{1-\alpha_i} - m_i^{1-\alpha_i} \right) \right] \frac{1-\alpha_{n-1}}{A\cdot k_i} + m_{n-1}^{1-\alpha_{n-1}} \right\}^{\frac{1}{1-\alpha_{n-1}}} \\ \text{if } \sum_{i=1}^{n-2} \frac{A\cdot k_i}{1-\alpha_i} \left(m_{i+1}^{1-\alpha_i} - m_i^{1-\alpha_i} \right) \leqslant y < \sum_{i=1}^{n-1} \frac{A\cdot k_i}{1-\alpha_i} \left(m_{i+1}^{1-\alpha_i} - m_i^{1-\alpha_i} \right) = 1 \end{cases} \tag{2.23}$$

where y is a random number in range [0,1] and $F^{-1}(y)$ is the inverse of the NCDF.

The Kroupa IMF [31] is a version of BPL chosen here to initialize the masses of cluster stars using McLuster in section 2.5.1.

2.2.2 Cluster Star Density Profile

Different density profiles (King [30], Plummer [48] and Elson, Fall & Freeman [18]) have been used ([27], [62], [26]) to simulate the physical characteristics of YMCs. The Plummer profile has been implemented here as described in [1] to generate positions and velocities for the stars within the cluster. At this stage the position and velocity of the center of mass is zero. In a second step the positions are offset to the desired location given as input parameter and the the circular velocity at that target location is added to the velocity of each star.

2.3 The Milky Way model

2.3.1 Galactic Potential

Modelling the gravitational potential of the Milky Way (MW) has been an ever evolving topic in recent decades. A brief history is given in [3]. Here the potential is used to approximate the force on the simulated stars and to initialize the parameters of the FSs.
The model of choice consists of four parts: black hole, bulge, disc and the dark matter halo.
The **black hole** is represented by a Keplerian potential:

$$\Phi_{bh}\left(r\right) = -\frac{G \cdot M_{bh}}{r} \tag{2.24}$$

with r being the spherical radius, with M_{bh} being the mass of the black hole, with G being the gravitational constant and with Φ_{bh} being the gravitational potential of the black hole.
The **disk** can be modelled via a Miyamoto Nagai potential [42]:

$$\Phi_{disk}\left(R, z\right) = -\frac{G \cdot M_{disk}}{\sqrt{R^2 + \left(a_{disk} + \sqrt{z^2 + b_{disk}^2}\right)^2}} \tag{2.25}$$

$$\rho_{disk}(R, z) = \frac{b_{disk}^2 M_{disk}}{4\pi} \frac{a_{disk} R^2 + \left[a_{disk} + 3(z^2 + b_{disk}^2)^{\frac{1}{2}}\right]\left[a_{disk} + (z^2 + b_{disk}^2)^{\frac{1}{2}}\right]^2}{\left\{R^2 + \left[a_{disk} + (z^2 + b_{disk}^2)^{\frac{1}{2}}\right]^2\right\}^{\frac{5}{2}} (z^2 + b_{disk}^2)^{\frac{3}{2}}} \tag{2.26}$$

with R being the cylindrical radius, with z being the distance to the reference plane, with a and b being scale parameters and ρ being the mass density.
For the **bulge** the Hernquist potential [28] is used:

$$\Phi_{bulge}\left(r\right) = -\frac{G \cdot M_{bulge}}{(r + a_{bulge})} \tag{2.27a}$$

$$\rho_{bulge}(r) = \frac{M_{bulge}}{2\pi} \frac{a_{bulge}}{r} \frac{1}{(r + a_{bulge})^3} \tag{2.27b}$$

a being the scale-length of the spheroid potential
and the Navarro–Frenk–White (NFW) potential [43] is used for the **dark matter halo** potential

$$\Phi_{halo}\left(r\right) = \frac{-4\pi G \rho_s r_s^3 \ln\left(1 + \frac{r}{r_s}\right)}{r} \tag{2.28}$$

Parameter	Value	Unit
M_{bh}	$4.0 \cdot 10^6$	$\mathrm{M}_\odot$
M_{disk}	$1.0 \cdot 10^{11}$	$\mathrm{M}_\odot$
a_{disk}	6.5	kpc
b_{disk}	0.26	kpc
M_{bulge}	$3.4 \cdot 10^{10}$	$\mathrm{M}_\odot$
a_{bulge}	0.70	kpc
r_s	16	kpc

Table 2.1: MW model hardcoded parameters. These parameters are listed here because they can not be changed by the user.

where ρ_s is the characteristic density and r_s the scale length.
Parameters for bulge and disk were taken from [52] and the radius r_s for the halo from [9]:
The gravitational potential of the MW model the sum of its components:

$$\Phi\left(R, z\right) = \Phi_{bh}\left(R, z\right) + \Phi_{disk}\left(R, z\right) + \Phi_{bulge}\left(R, z\right) + \Phi_{halo}\left(R, z\right) \tag{2.29}$$

ρ_s can be determined by imposing

$$v_c\left(R_0, z = 0\right) = 220\,\mathrm{km\,s^{-1}} \tag{2.30}$$

$$R_0 = 8\,\mathrm{kpc} \tag{2.31}$$

where v_c is the circular velocity and R_0 some fixed radial distance from the GC taken from [10].

Circular Velocity

The initial circular velocity v_c of a cluster around the GC is defined via

$$v_c\left(R, z\right) = \sqrt{R\frac{\partial\Phi\left(R, z\right)}{\partial R}} \tag{2.32}$$

where R is the radial distance from the GC and Φ the total potential as given in Equation 2.29. Therefore

$$v_c^2 = v_{c,bh}^2 + v_{c,disk}^2 + v_{c,bulge}^2 + v_{c,halo}^2 \tag{2.33}$$

where the individual velocity components are given by the following four equations:

$$v_{c,bh}^2 = \frac{GM_{bh}R^2}{\left(R^2 + z^2\right)^{3/2}} \tag{2.34}$$

$$v_{c,disk}^2 = \frac{GM_{disk}R^2}{\left(\left(a_{disk} + \sqrt{b_{disk}^2 + z^2}\right)^2 + R^2\right)^{3/2}} \tag{2.35}$$

$$v_{c,bulge}^2 = \frac{GM_{bulge}R^2}{\sqrt{R^2 + z^2}\left(a_{bulge} + \sqrt{R^2 + z^2}\right)^2} \tag{2.36}$$

$$v_{c,halo}^2 = \frac{4\pi G\rho_s R^2 r_s^3 \log\left(\frac{\sqrt{R^2+z^2}}{r_s} + 1\right)}{\left(R^2 + z^2\right)^{3/2}} - \frac{4\pi G\rho_s R^2 {r_s}^2}{\left(R^2 + z^2\right)\left(\frac{\sqrt{R^2+z^2}}{r_s} + 1\right)} \tag{2.37}$$

The circular velocity can be used for fitting the ρ_s model parameter [2]. Inserting the parameters given in Table 2.3.1 and setting $G \approx 4.302 \times 10^{-6}\,\mathrm{kpc\,M_\odot}^{-1}\,\mathrm{km}^2\,\mathrm{s}^{-2}$ results in $\rho_s \approx 4.5 \times 10^6\,\mathrm{M_\odot\,kpc^{-3}}$.
Fig. 2.2 displays the velocity for the chosen model and its components.

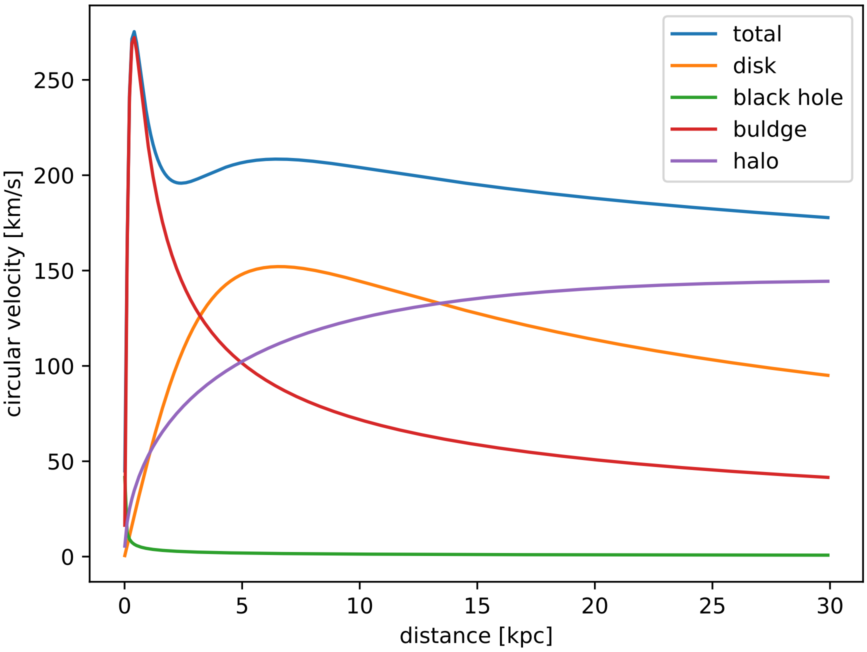

Figure 2.2: Galactic rotation curve derived from the model of the Milky Way used in this thesis. The top blue curve is a combination of all component velocity curves. The actual Milky Way rotation curve based on observational data oscillates between 200 and 250 km/s. Therefore the galactic rotation curve used in the simulation model is within realistic observational limits.

Angular Velocity

The initial angular velocities of the disc star are obtained from the potential:

$$\Omega^2\left(R\right) = \frac{1}{R}\frac{\partial\Phi\left(R,0\right)}{\partial r} \tag{2.38}$$

For the total potential (2.29) this derivation yields:

$$\begin{aligned}\Omega^2\left(R\right) = \frac{G}{R}\Bigg\{&-\frac{M_{bulge}}{\left(a_{bulge}+R\right)^2} + \frac{2M_{disk}R^3}{\left[\left(a_{disk}+b_{disk}\right)^2+R^4\right]^{1.5}}\\&+\frac{M_{bh}}{R^2} - \frac{4\pi p_s r_s^3}{R^2+Rr_s} + \frac{4\pi p_s r_s^3 \ln\left(\frac{R+r_s}{r_s}\right)}{R^2}\Bigg\}\end{aligned} \tag{2.39}$$

Mass Distribution

The mass inside a volume is calculated by numerical integration of the density. For this a GSL implementation of a Monte Carlo Integration is used. For further details refer to the GSL documentation. FSs masses are sampled from their respective mass function until the total sampled mass matches the total mass inside the cone of vision.

Surface Mass Density

The surface mass density Σ is used to estimate the vertical velocity dispersion of disc stars (2.94) and is defined by

$$\Sigma\left(R\right) = 2\int_0^\infty \rho\left(R,z\right)\mathrm{d}z \tag{2.40}$$

where z is the axial coordinate.

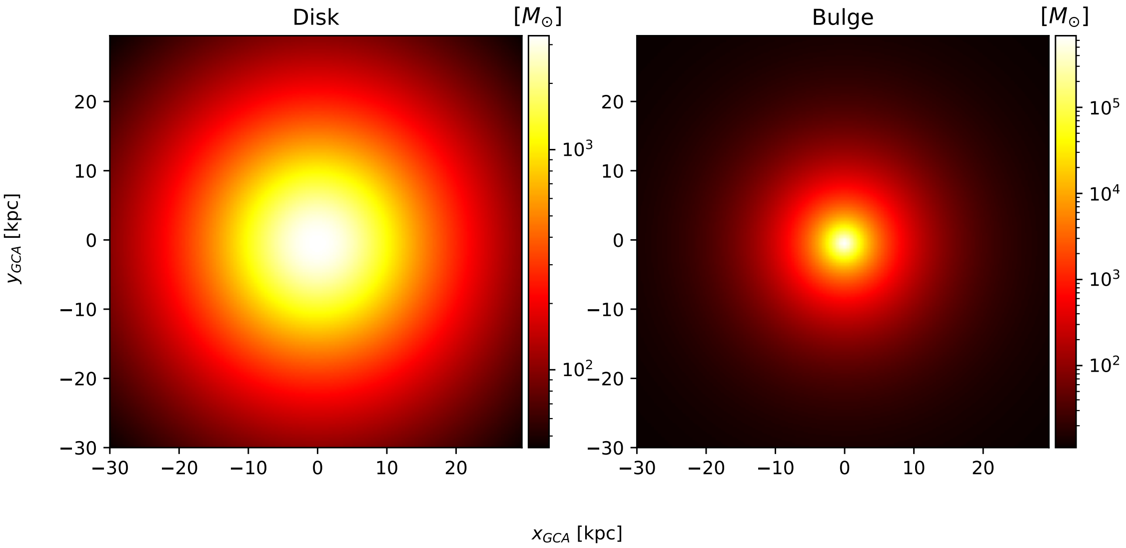

Figure 2.3: Mass in cubes with side length $100\,\mathrm{pc}$ of a horizontal slice through the Milky Way model between $z_{GCA} = 1.0\,\mathrm{kpc}$ to $1.1\,\mathrm{kpc}$. The displayed x_{GCA} and y_{GCA} are the lower bound of the cube. The bulge (right) covers a smaller area in the xy-plane but has a much higher density compared to the disk (left).

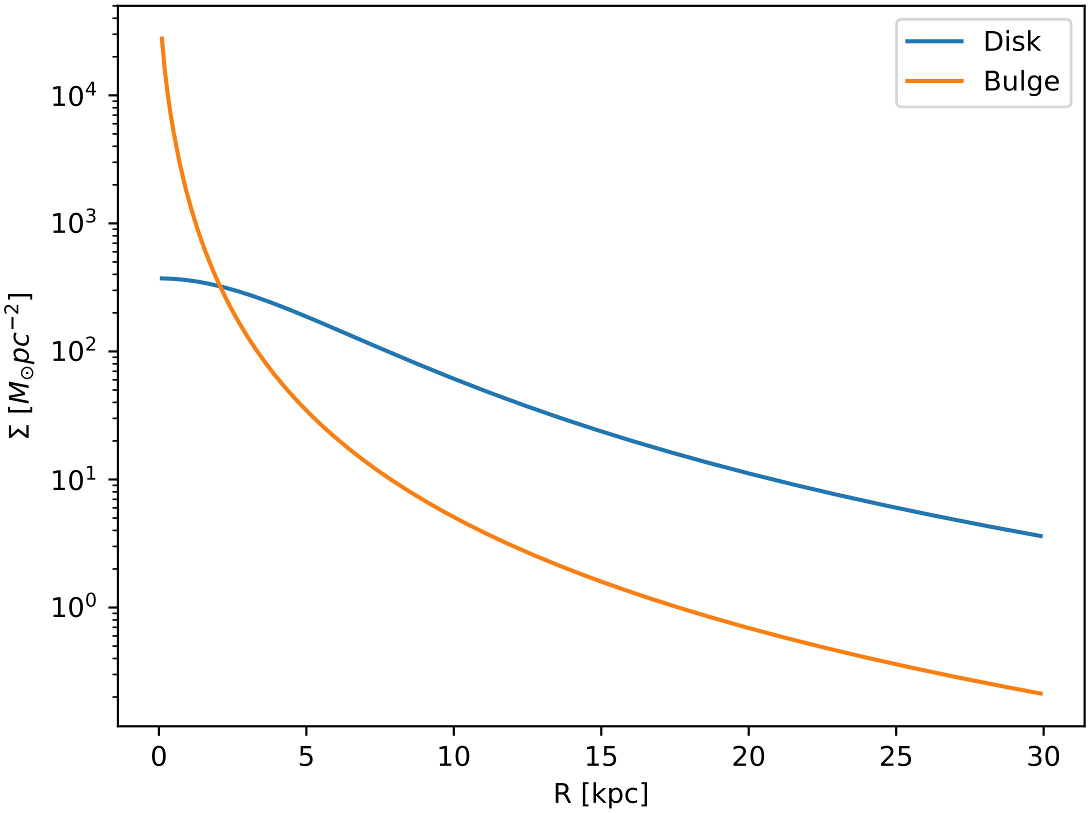

Figure 2.4: The radial surface mass density profiles of the Milky Way's disc and bulge components with increasing distance from the galactic centre. This figure shows a 1D abstraction of the 2D profiles shown in Figure 2.3

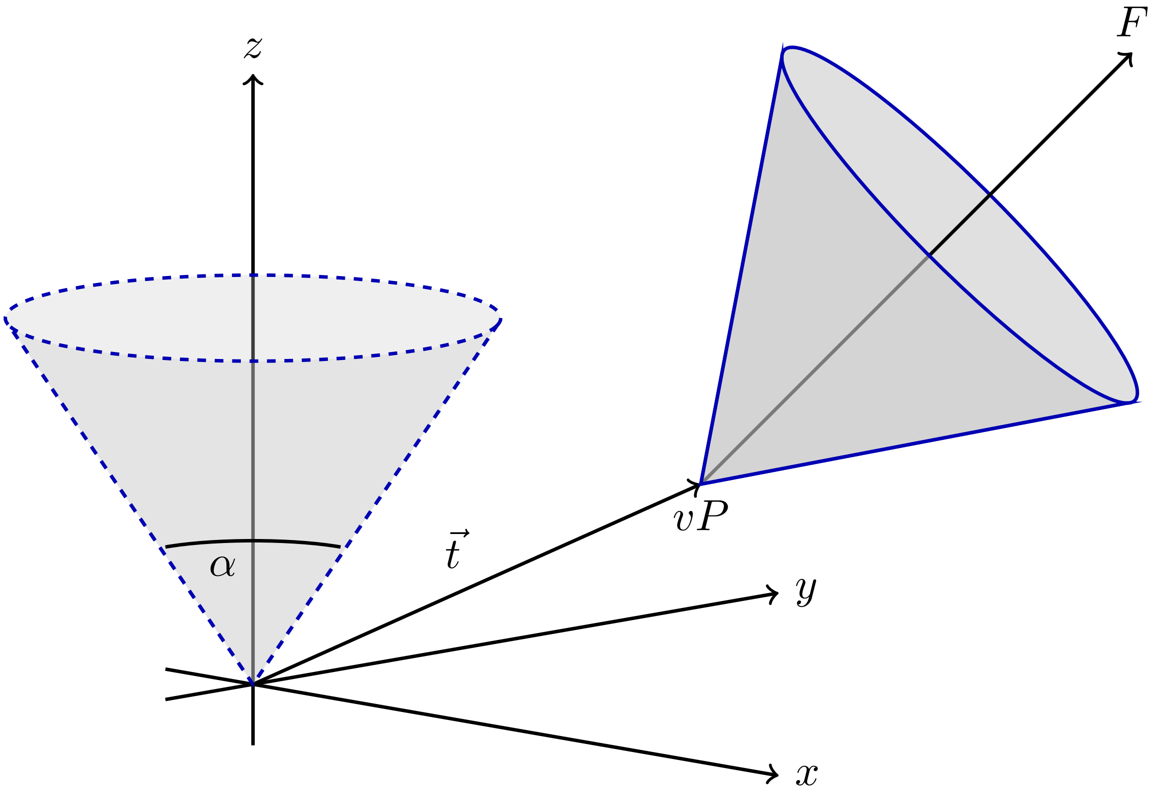

Figure 2.5: Transformation of the cone of vision. Trial positions for FS are generated by sampling from the z-Axis aligned cone volume (left) using a mass density profile akin to that of the desired observation direction within the Milky Way. A position transformation is applied to the FS sample set leading to the positions falling within the volume of the focus F aligned cone (right). The focus cone corresponds to the desired observation direction within the Milky Way.

2.3.2 Field Stars

Any star which does not belong to the simulated cluster is a field star (FS) and sampled from the disc and bulge potential described in subsection 2.3.1.

The cone of vision (COV) is defined by the angle of view α, the view distance h (height of the cone), the view point vP (location of the observer) and the focus F (a point along the line of sight).

The COV is constructed by transforming a right circular cone, where the vertex is at the origin and the circular base normal to the z axis.

Per transformation the tip of the cone is displaced from the origin to the view point vP and its axis is rotated to align with the line of sight l. Consequently, the transformation consists of both translation and rotation illustrated in Figure 2.5.

Rotation and translation are both isometric transformations meaning area and volume of the cone are preserved [23] (p.175).

A unit quaternion **q** is used in order to construct the rotation matrix. With rotation axis $\vec{b}$ and angle β the quaternion is given by

$$\mathbf{q} = \left(\cos\left(\frac{\beta}{2}\right), \vec{b}\,\sin\left(\frac{\beta}{2}\right)\right) \tag{2.41}$$

The rotation axis $\vec{b}$ is the normalized cross product of the original ($\vec{z}$) and target (l) cone axis

$$\vec{b} = \frac{\vec{z} \times \vec{l}}{\left\| \vec{z} \times \vec{l} \right\|} \tag{2.42}$$

The angle β between the vectors of interest can be calculated as follows

$$\beta = \text{atan2}\left(\tan\left(\beta\right)\right) = \text{atan2}\left(\frac{\sin\left(\beta\right)}{\cos\left(\beta\right)}\right) = \text{atan2}\left(\frac{\left\| \vec{z} \times \vec{l} \right\|}{\vec{z} \cdot \vec{l}}\right) \tag{2.43}$$

Next, the quaternion is converted to the rotation matrix [36]. Using the homogeneous notation [61] (p. 57) the matrix becomes:

$$\mathbf{R} = \begin{bmatrix} q_1^2 + q_2^2 - q_3^2 - q_4^2 & -2q_1q_4 + 2q_2q_3 & 2q_1q_3 + 2q_2q_4 & 0 \\ 2q_1q_4 + 2q_2q_3 & q_1^2 - q_2^2 + q_3^2 - q_4^2 & -2q_1q_2 + 2q_3q_4 & 0 \\ -2q_1q_3 + 2q_2q_4 & 2q_1q_2 + 2q_3q_4 & q_1^2 - q_2^2 - q_3^2 + q_4^2 & 0 \\ 0 & 0 & 0 & 1 \end{bmatrix} \tag{2.44}$$

The translation matrix for the translation vector $\vec{t}$ reads [61] (p. 66):

$$\mathbf{T_{translation}} = \begin{bmatrix} 1 & 0 & 0 & t_x \\ 0 & 1 & 0 & t_y \\ 0 & 0 & 1 & t_z \\ 0 & 0 & 0 & 1 \end{bmatrix} \tag{2.45}$$

The transformation matrix $\mathbf{T}$ is the product of $\mathbf{R}$ and $\mathbf{T_{translation}}$

$$\mathbf{T} = \begin{bmatrix} q_1^2 + q_2^2 - q_3^2 - q_4^2 & -2q_1q_4 + 2q_2q_3 & 2q_1q_3 + 2q_2q_4 & t_x \\ 2q_1q_4 + 2q_2q_3 & q_1^2 - q_2^2 + q_3^2 - q_4^2 & -2q_1q_2 + 2q_3q_4 & t_y \\ -2q_1q_3 + 2q_2q_4 & 2q_1q_2 + 2q_3q_4 & q_1^2 - q_2^2 - q_3^2 + q_4^2 & t_z \\ 0 & 0 & 0 & 1 \end{bmatrix} \tag{2.46}$$

The total mass M of disc and bulge stars is obtained by integrating the respective density over the COV.
For a right circular cone

$$\tan\left(\frac{\alpha}{2}\right) = \frac{R}{h} \tag{2.47}$$

and on its surface

$$\tan\left(\frac{\alpha}{2}\right) = \frac{r}{z} \tag{2.48}$$

$$z = \frac{h}{R} r \tag{2.49}$$

where R is the base radius of the cone and $r = \sqrt{x^2 + y^2}$. Hence $\frac{h}{R} r \leq z \leq h$. Both x and y are bound by the base radius. Choosing $|x| \leq R$ implies $|y| \leq \sqrt{R^2 - x^2}$.

$$M = \int_{-R}^{R} \int_{-\sqrt{R^2 - x^2}}^{\sqrt{R^2 - x^2}} \int_{\frac{h}{R} r}^{h} \rho\left(\mathbf{T} \cdot \begin{pmatrix} x \\ y \\ z \end{pmatrix}\right) dzdydx \tag{2.50}$$

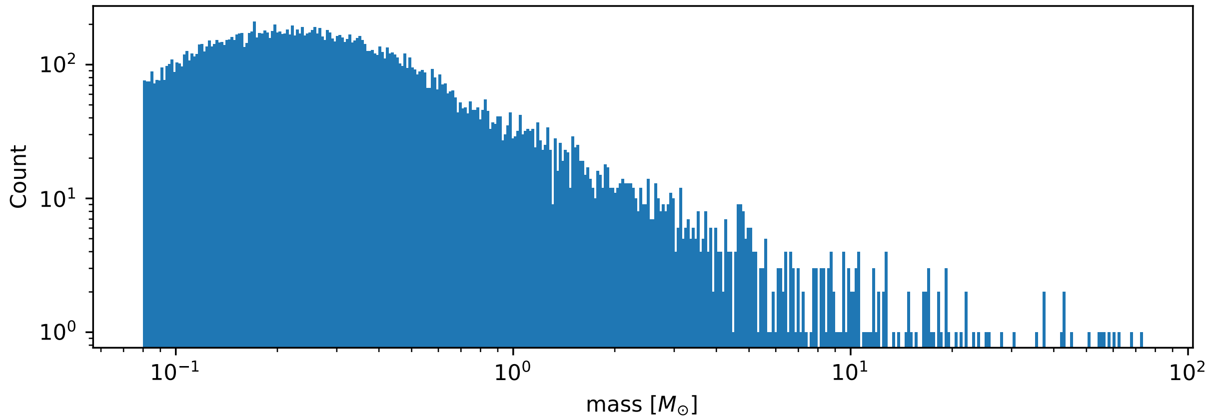

Figure 2.6: 10^3 stars sampled from the bulge PDMF which illustrates the difference in mass distribution compared to disc stars in Figure 2.7. This figure is included to demonstrate the accuracy of the author's implementation of the Milky Way's bulge present day stellar mass function.

Bulge Stellar Mass Function

By rejection sampling the function based on equation (2.51), given by [14], the mass of bulge stars is determined.
For $m < 0.7\,\mathrm{M}_\odot$ the log-normal distribution equation (2.51) is used. Parameters are $A = 3.6 \cdot 10^{-4}$, $m_c = 0.22$ and $\sigma = 0.33$. For $m > 0.7\,\mathrm{M}_\odot$ a Salpeter slope (2.14) with parameters $A = 7.1 \cdot 10^{-5}$ and $x = 1.3$ is chosen.
Samples are drawn until the sum of all samples $M_s = \sum_{i=1}^{n} m_i$ is larger than the total mass M. If $\sum_{i=1}^{n-1} m_i + \frac{m_n}{2} > M$ the last sample is removed.
Figure 2.6 show the mass distribution of a sample of bulge stars. Due to the different domains of the function the implementation is not trivial.

Disk Stellar Mass Function

Stars belonging to the disk are given a mass by rejection sampling the PDMF as given by [14].
For $m < 1\,\mathrm{M}_\odot$ the PDMF reads

$$\xi\left(\log(m)\right) = \frac{\mathrm{dN}}{\mathrm{dlog}(m))} = A \cdot \exp[\frac{-(\log(m) - \log(m_c))^2}{2\sigma^2}] \tag{2.51}$$

where ξ is the probability of stars having mass in range dm and dN is the number of stars within that range.
Equivalently (this version is sampled)

$$\xi\left(m\right) = \frac{\mathrm{dN}}{\mathrm{dm}} = \frac{A}{m\ln(10)} \cdot \exp[\frac{-(\log(m) - \log(m_c))^2}{2\sigma^2}] \tag{2.52}$$

For $m > 1\,\mathrm{M}_\odot$ the PDMF has the form

$$\xi\left(\log(m)\right) = \frac{\mathrm{dN}}{\mathrm{dlog}(m))} = Am^{-x} \tag{2.53}$$

or depending on m rather than $\log(m)$

$$\xi\left(m\right) = \frac{\mathrm{dN}}{\mathrm{dm}} = \frac{A}{m\ln(10)} m^{-x} \tag{2.54}$$

Figure 2.7 show the mass distribution of disk stars and confirms the correct implementation of the function in the code.

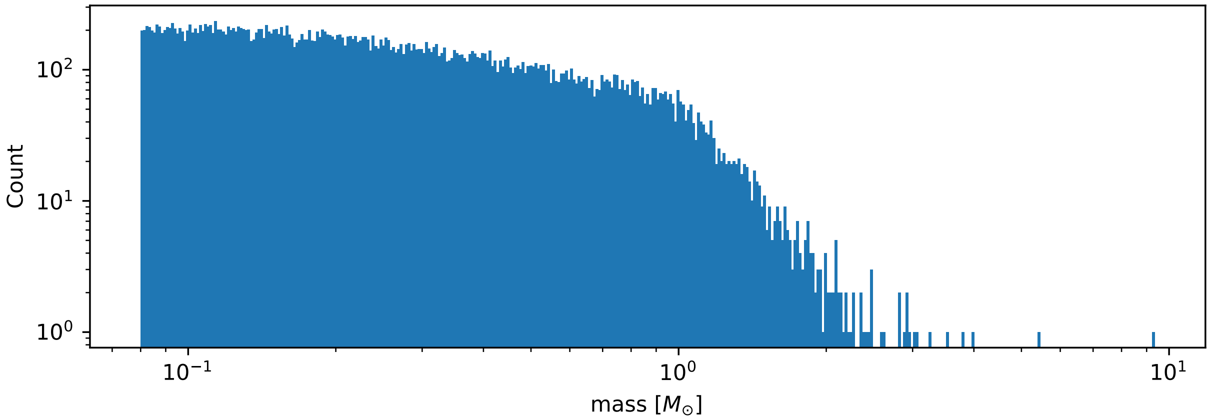

Figure 2.7: Stars with total mass of $10^3 M_\odot$ sampled from disk PDMF showcasing the difference to Figure 2.6

Field Star Positions

The positions of the FSs within the cone of vision are generated in two steps of rejection sampling followed by the line-of-sight transformation (2.46).
In the first step trial positions are drawn from a uniform distribution within a cuboid containing the cone. The boundaries of the cuboid are given by:

$$\begin{aligned} |x| &\leq R \\ |y| &\leq R \\ 0 \leq z &\leq h \end{aligned} \tag{2.55}$$

where $R = h \cdot \tan\left(\frac{\alpha}{2}\right)$ is the base radius , h is the height and α is the apex angle of the cone.
These trial positions are rejected in case they lie outside the boundaries of the cone. The conditions for acceptance are:

$$\begin{aligned} \sqrt{x^2+y^2} &\leq R \\ z &\geq h \cdot \frac{\sqrt{x^2+y^2}}{R} \end{aligned} \tag{2.56}$$

This method ensures that the positions are indeed homogeneously distributed, which is essential for the second step.
The second step consists of rejection sampling the density distribution. A random number is drawn from a uniform distribution ranging from the smallest to the largest possible density within the cone volume. If this number is smaller than the density at the trial position generated in step two, the trial position is accepted and rejected otherwise.
Finally, the accepted position is transformed via the transformation matrix (2.46).

Field Star Velocities

Particle Kinematics in Cylindrical Coordinates In terms of Cartesian unit vectors e_x,e_y and e_z, cylindrical unit vectors are given by

$$\begin{aligned} \hat{e}_R &= \hat{e}_x \cos(\phi) + \hat{e}_y \sin(\phi) \\ \hat{e}_\phi &= -\hat{e}_x \sin(\phi) + \hat{e}_y \cos(\phi) \\ \hat{e}_z &= \hat{e}_z \end{aligned} \tag{2.57}$$

where ϕ is the angle between the projection of a vector onto the xy-plane and the positive x-axis.

Since $\hat{e}_R$ depends on ϕ, position vectors have the form:

$$\vec{q} = R\hat{e}_R + z\hat{e}_z \tag{2.58}$$

The derivation by time gives the velocity:

$$\vec{v} = \dot{R}\hat{e}_R + R\dot{\phi}\hat{e}_\phi + \dot{z}\hat{e}_z \tag{2.59}$$

Lagrangian with axisymmetric potential Using (2.59) the Lagrangian (L)per unit mass reads:

$$L = \frac{1}{2}\left(\dot{R}^2 + R^2\dot{\phi}^2 + \dot{z}^2\right) + \Phi\left(R, z\right) \tag{2.60}$$

and using the Euler–Lagrange equation gives the conjugate momenta:

$$\begin{aligned} p_R &= \frac{\partial L}{\partial \dot{R}} = \dot{R} \\ p_\phi &= \frac{\partial L}{\partial \dot{\phi}} = R^2\dot{\phi} \\ p_z &= \frac{\partial L}{\partial \dot{z}} = \dot{z} \end{aligned} \tag{2.61}$$

Hamiltonian with axisymmetric potential Using the momenta in cylindrical coordinates (2.61) the Hamiltonian per unit mass with an axisymmetric potential reads [8] (p. 278):

$$H = \frac{1}{2}\left(p_R^2 + \frac{p_\phi^2}{R^2} + p_z^2\right) + \Phi\left(R, z\right) \tag{2.62}$$

using Hamilton's equations gives:

$$\dot{p}_R = -\frac{\partial H}{\partial R} = \frac{p_\phi^2}{R^3} - \frac{\partial \Phi}{\partial R} \tag{2.63}$$

$$\dot{p}_\phi = -\frac{\partial H}{\partial \phi} = -\frac{\partial \Phi}{\partial \phi} = 0 \tag{2.64}$$

$$\dot{p}_z = -\frac{\partial H}{\partial z} = -\frac{\partial \Phi}{\partial z} \tag{2.65}$$

Since $\vec{L} = \vec{p} \times \dot{\vec{p}}$ and thus:

$$L_z = R^2\dot{\phi} \tag{2.66}$$

Equation 2.64 signifies that, in the case of an axisymmetric potential, the z component of the angular momentum is conserved.

The phase space distribution function (DF) A galaxy can be viewed as a number of stars in phase space. The phase space is a six dimensional space spanned by position $\vec{q}$ and momentum $\vec{p}$. One point in phase space can therefore be described by a six dimensional vector $\vec{w} = (\vec{q}, \vec{p})$, the state of a whole galaxy as a DF $f(\vec{q}, \vec{p}, t)$. $f(\vec{q}, \vec{p}, t)d^3\vec{q}d^3\vec{p}$ is the probability that some specific star is inside the 6D cuboid defined by $d^3\vec{q}d^3\vec{p}$ at time t.
The conservation of probability in phase space is, similarly to the continuity equation in fluid dynamics, given by

$$\frac{\partial f}{\partial t} + \sum_{i=1}^{6} \frac{\partial}{\partial w_i}(f\dot{w}_i) = 0 \tag{2.67}$$

with $\dot{\vec{w}} = (\dot{\vec{q}}, \dot{\vec{p}})$.
The right summand can be changed as follows, using Hamilton equations

$$\begin{aligned}
\sum_{i=1}^{6} \frac{\partial}{\partial w_i}(f \dot{w}_i) &= \sum_{i=1}^{3} \left(\frac{\partial}{\partial q_i}(f \dot{q}_i) + \frac{\partial}{\partial p_i}(f \dot{p}_i) \right) \\
&= \sum_{i=1}^{3} \left(\frac{\partial}{\partial q_i} \left(f \frac{\partial H}{\partial p_i} \right) - \frac{\partial}{\partial p_i} \left(f \frac{\partial H}{\partial q_i} \right) \right) \\
&= \sum_{i=1}^{3} \left(\frac{\partial f}{\partial q_i} \frac{\partial H}{\partial p_i} + f \frac{\partial^2 H}{\partial q_i \partial p_i} - \frac{\partial f}{\partial p_i} \frac{\partial H}{\partial q_i} - f \frac{\partial^2 H}{\partial p_i \partial q_i} \right) \\
&= \sum_{i=1}^{3} \left(\frac{\partial f}{\partial q_i} \frac{\partial H}{\partial p_i} - \frac{\partial f}{\partial p_i} \frac{\partial H}{\partial q_i} \right)
\end{aligned} \tag{2.68}$$

And therefore

$$\frac{\partial f}{\partial t} + \sum_{i=1}^{3} \left(\frac{\partial f}{\partial q_i} \frac{\partial H}{\partial p_i} - \frac{\partial f}{\partial p_i} \frac{\partial H}{\partial q_i} \right) = 0 \tag{2.69}$$

which is the collisionless Boltzmann Equation (CBE).
The zeroth moment of the DF is the number density:

$$\nu(\vec{x}) \equiv \int f(\vec{x}, \vec{v}) d^3\vec{v} \tag{2.70}$$

Mean velocities are given by the first moment:

$$\overline{v_i}(\vec{x}) \equiv \frac{1}{\nu(\vec{x})} \int v_i f(\vec{x}, \vec{v}) d^3\vec{v} \tag{2.71}$$

Jeans equations Using Einstein notation for $i = 1, 2, 3$ the CBE (2.69) is given by [8] (p. 277):

$$\frac{\partial f}{\partial t} + \frac{\partial f}{\partial q_i} \frac{\partial H}{\partial p_i} - \frac{\partial f}{\partial p_i} \frac{\partial H}{\partial q_i} = 0 \tag{2.72}$$

Since the galactic potential (2.29) is axisymmetric, it is convenient to express this equation in cylindrical coordinates.

$$\frac{\partial f}{\partial t} + p_R \frac{\partial f}{\partial R} + \frac{p_\phi}{R^2} \frac{\partial f}{\partial \phi} + p_z \frac{\partial f}{\partial z} - \left(\frac{\partial \Phi}{\partial R} - \frac{p_\phi^2}{R^3} \right) \frac{\partial f}{\partial p_R} - \frac{\partial \Phi}{\partial \phi} \frac{\partial f}{\partial p_\phi} - \frac{\partial \Phi}{\partial z} \frac{\partial f}{\partial p_z} = 0 \tag{2.73}$$

It is assumed that the galaxy is statistically in a steady state [6] i.e. $\frac{\partial f}{\partial t} = 0$. Due to this assumption and taking (2.64) into account (2.73) simplifies to

$$p_R \frac{\partial f}{\partial R} + \frac{p_\phi}{R^2} \frac{\partial f}{\partial \phi} + p_z \frac{\partial f}{\partial z} - \left(\frac{\partial \Phi}{\partial R} - \frac{p_\phi^2}{R^3} \right) \frac{\partial f}{\partial p_R} - \frac{\partial \Phi}{\partial z} \frac{\partial f}{\partial p_z} = 0 \tag{2.74}$$

Multiplying equation (2.74) by p_R and integrating over all momenta leads to

$$\frac{\partial \nu \overline{v_R^2}}{\partial R} + \frac{\partial \nu \overline{v_R v_z}}{\partial z} + \nu \left(\frac{\overline{v_R^2} - \overline{v_\phi^2}}{R} + \frac{\partial \Phi}{\partial R} \right) = 0 \tag{2.75}$$

Equation 2.75 is significant because it is the basis for initialising the disk star velocities, as described in section 2.3.2.

The Epicyclic Approximation Individual stars in the disk are on nearly circular orbits. Such orbits can be approximated by circular orbits with additional retrograde elliptical orbits around the guiding center.
The derivation of this approximation starts with Hamilton's equations for an axisymmetric potential.
Rearranging (2.62) and using (2.66) gives:

$$H = \frac{1}{2}\left(p_R^2 + p_z^2\right) + \frac{L_z^2}{2R^2} + \Phi\left(R, z\right) \tag{2.76}$$

With the effective potential given by:

$$\Phi_{\text{eff}}\left(R, z\right) = \frac{L_z^2}{2R^2} + \Phi\left(R, z\right) \tag{2.77}$$

This leads to:

$$H_{\text{eff}} = \frac{1}{2}\left(p_R^2 + p_z^2\right) + \Phi_{\text{eff}}\left(R, z\right) \tag{2.78}$$

Here $\frac{1}{2m}\left(p_R^2 + p_z^2\right)$ is the kinetic energy in the (R, z) plane or meridional plane. The angular momentum term in the effective potential is not a real potential energy even though it is sometimes called the centrifugal potential. It really is the angular kinetic energy. The given definition of Φ_{eff} is only valid because L_z is conserved.
Using Φ_{eff}, (2.63) and (2.65) can be written as

$$\dot{p}_R = -\frac{\partial \Phi_{\text{eff}}}{\partial R} \tag{2.79}$$

$$\dot{p}_z = -\frac{\partial \Phi_{\text{eff}}}{\partial z} \tag{2.80}$$

These equations describe harmonic oscillations in the effective potential. The minimum of effective potential is the minimum of the real potential energy, together with a contribution from the angular kinetic energy.

$$\begin{aligned} \frac{\partial \Phi_{\text{eff}}}{\partial R} = \frac{\partial \Phi}{\partial R} - \frac{L_z^2}{R^3} &= 0 \\ \frac{\partial \Phi_{\text{eff}}}{\partial z} &= 0 \end{aligned} \tag{2.81}$$

The first condition states that the attractive force $(-\frac{\partial \Phi_{\text{eff}}}{\partial R})$ has to balance the "centrifugal force". This is the condition for circular orbits with angular momentum L_z. The second condition is clearly satisfied in the equatorial plane $(z = 0)$. The coordinates of this guiding centre are defined as (R_g, ϕ_g, z_g).
In preparation for a Taylor series expansion about the guiding centre, x is defined as

$$x \equiv R - R_g \tag{2.82}$$

If $R = R_g$ then $x = 0$ and therefore the guiding centre is at $(x, z) = (0, 0)$.

$$\begin{aligned} \Phi_{\text{eff}} = \Phi_{\text{eff}}(R_g, 0) + \left.\frac{\partial \Phi_{\text{eff}}}{\partial R}\right|_{(R_g,0)} x + \left.\frac{\partial \Phi_{\text{eff}}}{\partial z}\right|_{(R_g,0)} z + \\ \frac{1}{2}\left.\frac{\partial^2 \Phi_{\text{eff}}}{\partial R^2}\right|_{(R_g,0)} x^2 + \frac{1}{2}\left.\frac{\partial^2 \Phi_{\text{eff}}}{\partial z^2}\right|_{(R_g,0)} z^2 + \frac{1}{2}\left.\frac{\partial^2 \Phi_{\text{eff}}}{\partial x \partial z}\right|_{(R_g,0)} xz + \mathcal{O}(xz^2) \end{aligned} \tag{2.83}$$

The first order terms are zero (since Φ_{eff} is minimized at the guiding centre) as is the xz term. The latter due to symmetry about $z = 0$.

In the epicyclic approximation terms of $\mathcal{O}(xz^2)$ and higher are neglected.
With this approximation (2.79) and (2.80) become

$$\dot{p}_x = -\frac{\partial \Phi_{\text{eff}}}{\partial x} \approx -\left.\frac{\partial^2 \Phi_{\text{eff}}}{\partial R^2}\right|_{(R_g,0)} x \equiv -\kappa^2 x \tag{2.84}$$

$$\dot{p}_z = -\frac{\partial \Phi_{\text{eff}}}{\partial z} \approx -\left.\frac{\partial^2 \Phi_{\text{eff}}}{\partial z^2}\right|_{(R_g,0)} z \equiv -\nu^2 z \tag{2.85}$$

where the epicyclic frequency κ is the frequency of small radial oscillations and the vertical frequency ν the frequency of small vertical oscillations.
With potential $\Phi\,(R,z)$ Eq. (2.84) can be written as

$$\kappa^2 = \left.\frac{\partial^2 \Phi}{\partial R^2}\right|_{(R_g,0)} + \frac{3L_z^3}{R_g^4} \tag{2.86}$$

The combination of (2.61) with: (2.63), given $\dot{p}_R = 0$ and by definition $\Omega = \dot{\phi}$, results in the circular angular frequency

$$\Omega^2 = \left.\frac{1}{R}\frac{\partial \Phi}{\partial R}\right|_{(R_g,0)} = \frac{L_z^2}{R^4} \tag{2.87}$$

The derivative of (2.87) is:

$$\frac{\partial^2 \Phi}{\partial R^2} = \Omega^2 + R\frac{d\Omega^2}{dR} \tag{2.88}$$

Inserting (2.87) and (2.88) into (2.86) yields:

$$\kappa^2(R_g) = \left.\left(R\frac{d\Omega^2}{dR} + 4\Omega^2\right)\right|_{R=R_g} \tag{2.89}$$

The variance, σ, is generally given as the mean of squares minus the square of means. In the epicyclic approximation the mean velocity in R and z is zero and therefore:

$$\begin{aligned} \sigma_{v_\phi}^2 &= \overline{v_\phi^2} - \overline{v_\phi}^2 \\ \sigma_{v_R}^2 &= \overline{v_R^2} \\ \sigma_{v_z}^2 &= \overline{v_z^2} \end{aligned} \tag{2.90}$$

Equation 2.90 is used to initialize the velocities of FSs belonging to the disk as described in section 2.3.2.

Disk field stars The velocity distribution of stars in the MW disk is approximated with the help of the Jeans equations as well as relations and constraints based on observations.
For a flat rotation curve the radial velocity dispersion exponentially decreases with increasing radius (see [60], p. 114)

$$\sigma_{v_R} \propto e^{-\frac{R}{h}} \tag{2.91}$$

where h in the case of the Miyamoto Nagai potential is the radial scale length a.
The relation (2.91) still requires a constant factor k, which can be determined by means of the Toomre parameter Q at some distance R_{ref}.
Q is the ratio between the actual and minimum velocity dispersion $\sigma_{v_{R,min}}$ ([58], p. 1234)

$$\begin{aligned} \sigma_{v_{R,min}} &= \frac{3.36G\Sigma}{\kappa} \\ Q \equiv \frac{\sigma_{v_R}}{\sigma_{v_{R,min}}} &= \frac{\kappa\sigma_{v_R}}{3.36G\Sigma} \end{aligned} \tag{2.92}$$

where κ denotes the epicyclic frequency (2.89).
In the solar neighborhood $Q_* = 2.7 \pm 0.4$ and $\sigma_{v_R} = (38 \pm 2)\mathrm{km\,s^{-1}}$ [8] (p. 497)
The constant k can therefore be approximated via

$$k \cong Q\sigma_{v_{R,min}} e^{\frac{R}{h}} \tag{2.93}$$

Under the approximation of isothermal sheets (introduced in [60]), the vertical velocity dispersion only depends on the surface density [59]:

$$\sigma_{v_z} = \pi G \Sigma\left(R\right) z_0 \tag{2.94}$$

with z_0 being the vertical scale length, b, when using the Miyamoto Nagai potential.
Combining the equation for the circular velocity (2.32) with the Jeans equation (2.75) and multiplying by $\frac{R}{\nu}$ results in:

$$\frac{R}{\nu}\frac{\partial \nu \overline{v_R^2}}{\partial R} + \frac{R}{\nu}\frac{\partial \nu \overline{v_R v_z}}{\partial z} + \overline{v_R^2} - \overline{v_\phi^2} + v_c^2 = 0 \tag{2.95}$$

For a razor thin disc the spatial density ν can be replaced with the surface density Σ [29], which does not depend on z. By using relations (2.90), (2.95) this simplifies to

$$\frac{R}{\Sigma}\frac{\partial \nu \sigma_{v_R}^2}{\partial R} + R\frac{\partial \overline{v_R v_z}}{\partial z} + \sigma_{v_R}^2 - \sigma_{v_\phi}^2 - \overline{v_\phi}^2 + v_c^2 = 0 \tag{2.96}$$

In the epicyclic approximation, azimuthal and radial dispersion have the following relation ([8] p. 170):

$$\frac{\sigma_{v_\phi}^2}{\sigma_{v_R}^2} = \frac{\kappa^2}{4\Omega^2} \tag{2.97}$$

With this relation (2.96) can be written as:

$$\frac{R}{\Sigma}\frac{\partial\left(\Sigma\sigma_{v_R}^2\right)}{\partial R} + R\frac{\partial \overline{v_R v_z}}{\partial z} + \sigma_{v_R}^2 - \sigma_{v_R}^2\frac{\kappa^2}{4\Omega^2} - \overline{v_\phi}^2 + v_c^2 = 0 \tag{2.98}$$

Rearrangements lead to:

$$\overline{v_\phi}^2 - v_c^2 = \sigma_{v_R}^2\left(1 - \frac{\kappa^2}{4\Omega^2} + \frac{R}{\Sigma\sigma_{v_R}^2}\frac{\partial\left(\Sigma\sigma_{v_R}^2\right)}{\partial R} + \frac{R}{\sigma_{v_R}^2}\frac{\partial \overline{v_R v_z}}{\partial z}\right) \tag{2.99}$$

Due to the exponential dependency of the surface mass density ([8] p. 325) and the radial dispersion σ_{v_R} (2.91) on R, the derivation after R summand can be solved as follows:

$$\begin{gathered}\frac{R}{\Sigma\sigma_{v_R}^2}\frac{\partial\left(\Sigma\sigma_{v_R}^2\right)}{\partial R} = \frac{1}{\Sigma\sigma_{v_R}^2}\frac{\partial R}{\partial\ln(R)}\frac{\partial\left(\Sigma\sigma_{v_R}^2\right)}{\partial R} = \\ \frac{1}{\Sigma\sigma_{v_R}^2}\frac{\partial\left(\Sigma\sigma_{v_R}^2\right)}{\partial\ln(R)} = \frac{1}{\Sigma\sigma_{v_R}^2}\left(-\frac{R\Sigma\sigma_{v_R}^2}{a} - \frac{R\sigma_{v_R}^2\Sigma}{a}\right) = -2\frac{R}{a}\end{gathered} \tag{2.100}$$

Under the assumption that the retrograde elliptical orbit is aligned with the coordinate axes (2.99) becomes:

$$\overline{v_\phi}^2 - v_c^2 = \sigma_{v_R}^2\left(1 - \frac{\kappa^2}{4\Omega^2} - \frac{R}{a}\right) \tag{2.101}$$

The velocity components of stars can be sampled from Gaussian distributions. Dispersions are obtained by first evaluating the epicyclic frequency (2.89) and the surface mass density (2.40), followed by the radial velocity dispersion (2.91) with constant factor (2.93), the vertical (2.94) and the azimuthal velocity dispersion (2.97). As noted before, the mean velocity in R and z is zero. For ϕ the mean velocity is calculated from (2.101), where the circular velocity v_c is given by (2.32).

Bulge field stars For spherically symmetric distribution functions with the present approximations, the spherically symmetric Jeans equation can be used to determine the kinematic properties of the bulge field stars [64]:

$$\frac{\partial(\rho\sigma_r^2)}{\partial r} + 2\frac{\beta\sigma_r^2}{r} + \rho\frac{\partial\Phi}{\partial r} = 0 \tag{2.102}$$

where β is an indicator for anisotropy in the radial and tangential directions:

$$\beta = 1 - \frac{\sigma_\phi^2}{\sigma_r^2} \tag{2.103}$$

If the distribution is isotropic, as assumed here, $\beta = 0$ and (2.102) simplifies to:

$$\frac{\partial(\rho\sigma_r^2)}{\partial r} + \rho\frac{\partial\Phi}{\partial r} = 0 \tag{2.104}$$

and the radial dispersion can be calculated by integration:

$$\sigma_r^2 = \frac{1}{\rho}\int_r^\infty \rho\frac{\partial\Phi}{\partial r}\mathrm{dr} \tag{2.105}$$

However, Φ is the composite potential consisting of bulge, disc and halo and therefore not spherically symmetric. As suggested in [29], contribution by the disc to the bulge dispersion may be accounted for by spherically averaging the disc potential. This is achieved by expressing the cylinder in spherical coordinates and integrating over the relevant angle:

$$\sigma_{r,disk}^2 = \frac{1}{\rho}\int_r^\infty \frac{\rho}{2\pi}\int_0^{2\pi}\frac{\partial\Phi\left(r\sin(\theta), r\cos(\theta)\right)}{\partial r}\mathrm{d}\theta\mathrm{dr} \tag{2.106}$$

As neither of these integrals have an analytical solution, this calculation is computationally intensive. Therefore a lookup table has been implemented in which discrete values for r and corresponding bulge dispersion are stored.

Figure 2.8 shows a comparison of the results of simulations based on the derivations in this chapter (lines), and observational values of the MW from [35] (dots with error bars). Color-coding (red, green and blue) is used to differentiate between three different values for the latitude b.

These results were generated using a view distance of $7.5\,\mathrm{kpc}$. The other parameters are given in Table 2.3.1. The radial velocity dispersion heavily depends on the scale parameter of the bulge potential. With the current choice, the dispersion at small r is lower than realistic. This issue could be solved by adding an additional potential with smaller scale radius. A multi component bulge model has been suggested for instance by [53].

2.4 Data storage

A SQLite Database is used to store the output of simulations including all relevant model parameters, stars properties with their respective positions and velocities as well as data resulting from analysis. SQLite supports both C++ and python and is therefore used in most data related parts of the project. Generated data can be loaded and plotted directly from the database. Previously performed simulations can be loaded from the database in order to carry out analysis like energy vs time or average star velocity vs time.

Due to bad performance, no foreign key constraints where set for `position.id_star` and `velocity.id_star`. A multi-column index is used to improve the execution time of queries containing both `velocity.timestep` and `velocity.id_star`. `NULL` values are avoided where possible. However, at many stages during execution, some information is unknown, but creating entries is still required. Observed stars contain no information about their mass or GCA phase space coordinates. Additionally some observationally detected stars cannot be mapped to simulated stars, etc.

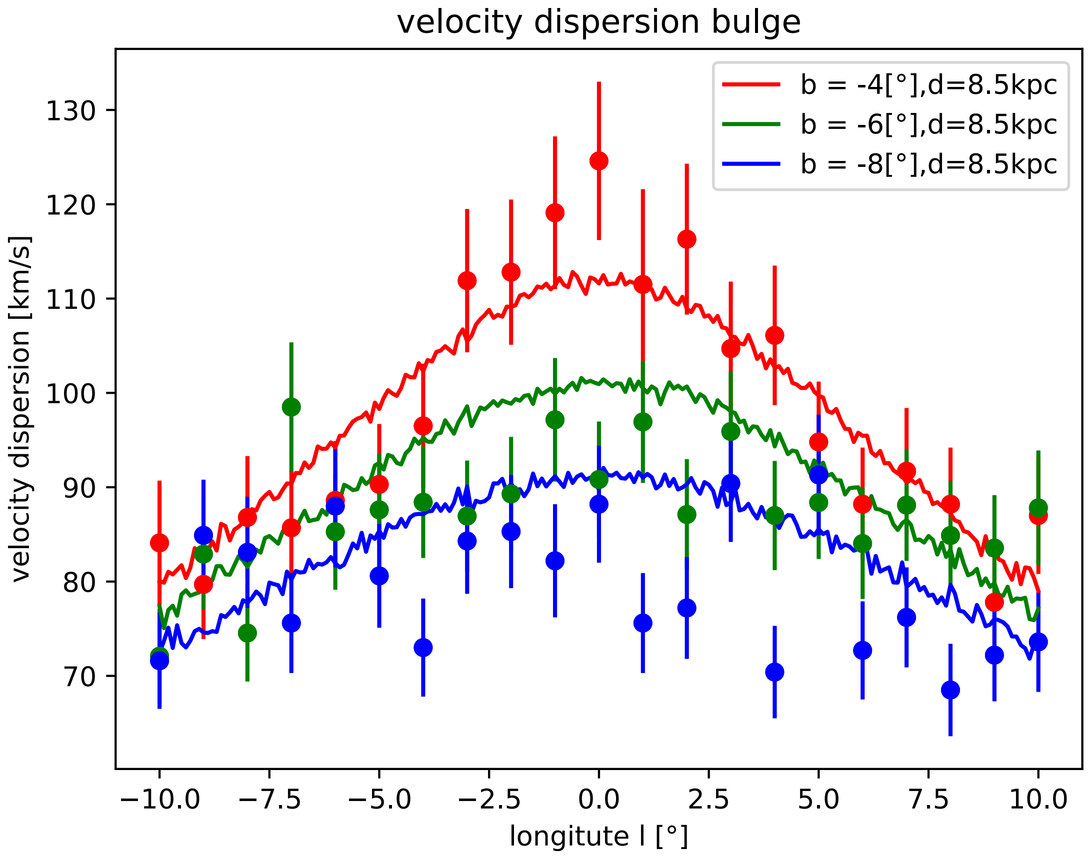

Figure 2.8: Velocity dispersion of bulge stars at different galactic longitudes. The solid lines represents result from simulations conducted for this thesis. The points with error bars are results from observations [24]. This plot shows that the author's implementation of the Milky Way potential leads to star velocity dispersions within the uncertainty estimates of observational data.

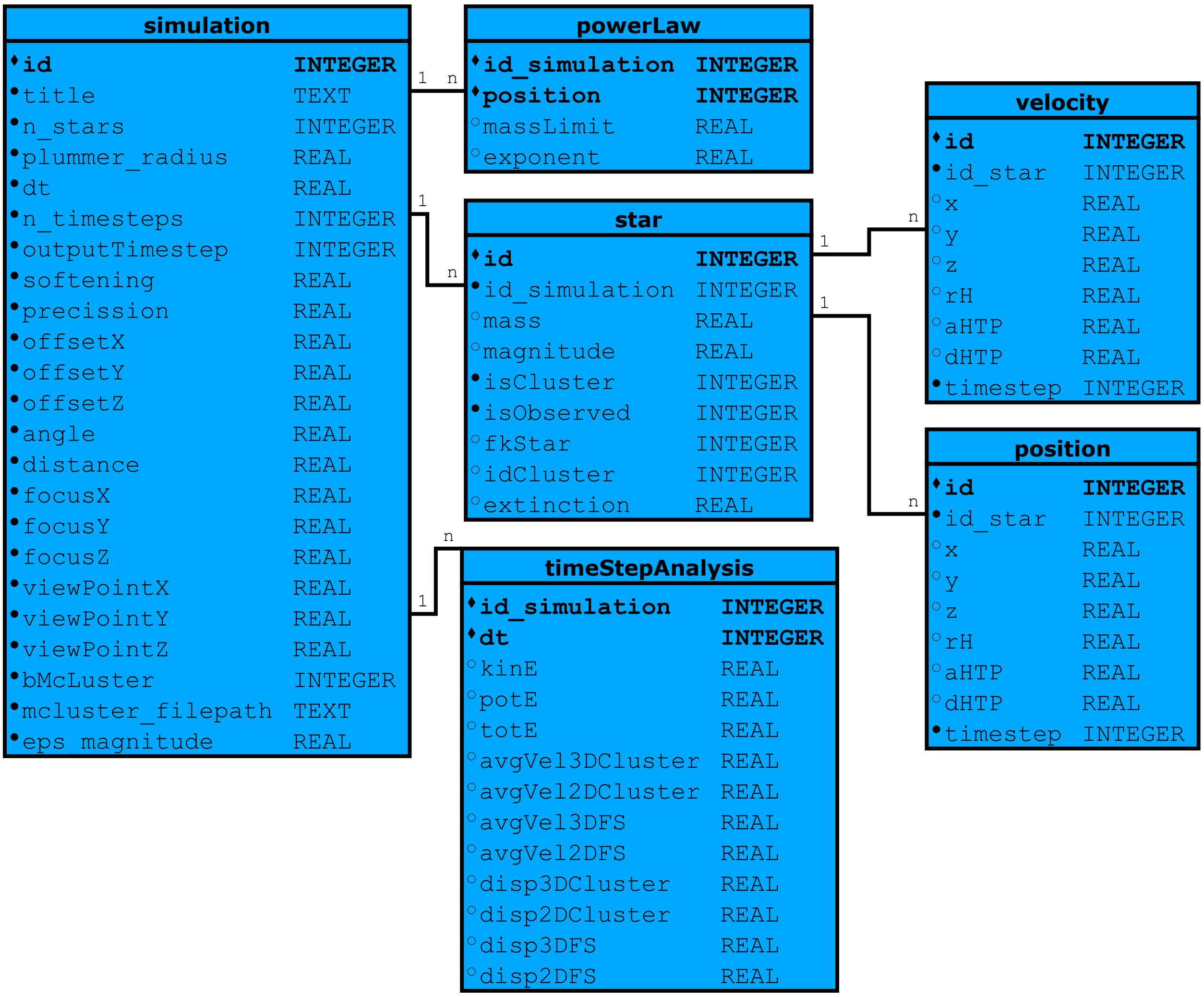

Figure 2.9: The database model for storing kinematic data of the simulated field stars and clusters. Generating simulated data sets is computationally expensive. Therefore the results of simulations with various initialization parameters are stored in a database that allows them to be efficiently recalled for future analysis.

2.4.1 Entity Relationship Diagram

When creating a database-driven application, it is advisable to start with the creation of a database model, as this is the basis of the application. Several steps are required, such as writing a text about the part of reality that the database represents, organising this text into entities that contain all relevant information and defining relationships between such entities. In practice this initial model may be a good first attempt but adjustments need to be made as the project evolves. Fig. 2.9 depicts the current model.
♦ are primary keys. The tables powerLaw and timeStepAnalysis have composite primary keys.
○ are nullable fields. Even star.mass is nullable since the mass of observed stars is not known.
• are not nullable fields. The simulation table exclusively contains such values since all these fields are required input parameters for the simulation.

2.5 Simulations

A total of 25 simulations with varying positions relative to the galactic centre and cluster masses were carried out in order to study the effects of these parameters on the performance of the cluster detection algorithm. The galactic coordinates were set to $l = 0^\circ$ and $b \in \{0, 5, 10, 25, 180\}$ $[^\circ]$ HGP. For each longitude five cluster masses $\in \{0.64, 1.6, 4.0, 10, 25\}$ [kM$_\odot$] were simulated. The

Longitude °	# FS	FS $\bar{v}$ $\mathrm{km\,s^{-1}}$	FS σ_v $\mathrm{km\,s^{-1}}$	CS $\bar{v}$ $\mathrm{km\,s^{-1}}$
0	351000	254	145	150
5	67500	380	178	182
10	47700	307	170	204
25	19800	172	107	242
180	687	219	4.91	215

Table 2.2: Summary of the field star (FS) properties for the five different simulated fields of view at different galactic longitudes with the Milky Way model. $\bar{v}$ is the average velocity and σ_v is the velocity dispersion of the stars in each simulated data set. The circular velocity of the cluster stars (CS) placed at 8 kpc along these lines of sight in the Milky Way potential model are also given.

lower angular steps near the GC are due to the fact that the stellar density decreases rapidly with increasing angular distance from the galactic centre. Each simulation was repeated 10 times for error estimation.

2.5.1 Parameters

The following parameters remained unchanged between the simulations.

General simulation parameters

- FOV angle: $54\,$arcsec
  Chosen large enough to cover most of the cluster stars. See α in Fig. 2.5. The upper limit is dictated by the available computer hardware. This choice still results in $\sim 3.5 \times 10^5$ FS with view direction towards the GC.

- View distance: $9\,\mathrm{kpc}$
  The height of the COV or line of sight distance reaching behind the GC when looking towards it.

- Cluster distance: $8\,\mathrm{kpc}$
  The distance between the observer and the cluster. When looking straight at the GC the distance between the cluster and the GC is $300\,\mathrm{pc}$
  The mean cluster velocity is set to the circular velocity at this location.

- View point: $(X, Y, Z) = (8300, 0, 27)\mathrm{pc}$
  The position of the observer in GCA.

- Timestep: $28\,\mathrm{d}$
  Amount of time between the two recorded snapshots. The time per integration is $7\,\mathrm{d}$. Therefore, snapshots are taken every 4 integrations. Setting the timestep size to one day results in an average CS velocity of $\sim 1 \times 10^{-4}\,$arcsec$\,\mathrm{d}^{-1}$. Since the diffraction limit of the ELT is $8 \times 10^{-3}\,$arcsec$\,\mathrm{px}^{-1}$ this timestep would be too small to register movement. The chosen timestep results in an average CS velocity of $\sim 2.2 \times 10^{-3}\,$arcsec$\,\mathrm{d}^{-1}$, which is still below the diffraction limit. However, the velocity has to be small enough to limit the number of wrong assignments during velocity estimation. That is, the displacement of one star between the two images should be small enough that it is not wrongfully matched to a nearby star moving in the opposite direction. Tests with a timestep size of $42\,\mathrm{d}$ did not lead to a significant increase in wrong assignments but at the same time did not improve the velocity estimation to a significant degree. After all the accuracy of the velocity estimation only matters in regards to differentiating between CS and FS.

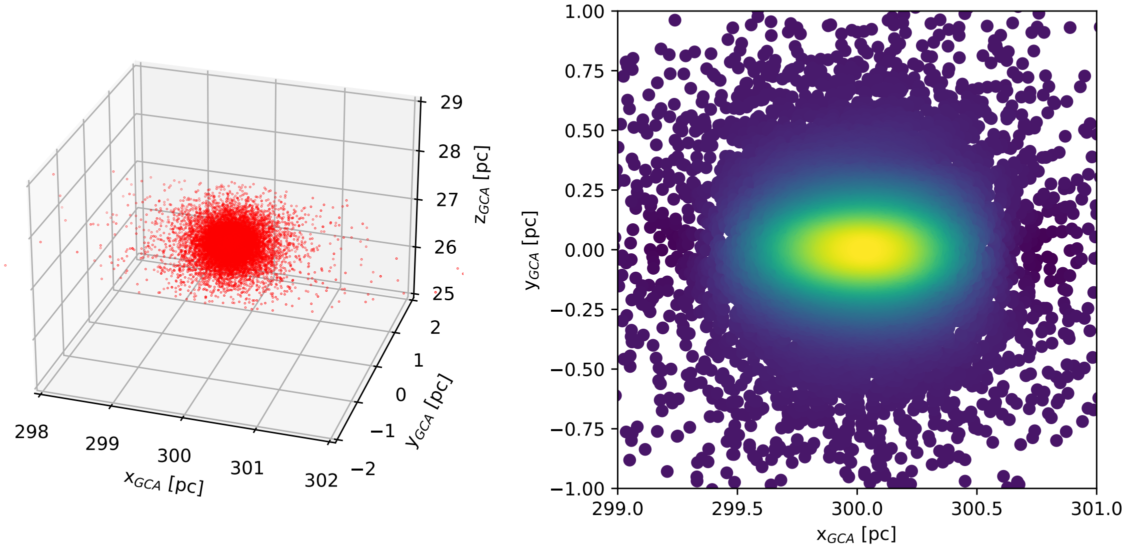

Figure 2.10: A simulated cluster 300 pc from the GC. Left: a point cloud showing the distribution of $\sim$17000 stars in a $10\,\mathrm{kM}_\odot$ young stellar cluster. Right: Projection of the points onto the xy-plane colored by point density.

Cluster specific parameters (McLuster)

- (P) Profile: 0 Plummer density profile

- (R) Radius: -1
  With this setting the radius is calculated by McLuster via a mass to half-mass radius relation as described in [38]

- (Q) Virial ratio: 0.5
  The cluster is in virial equilibrium.

- (f) IMF: 1
  Kroupa ranging from 0.08 $[\mathrm{M}_\odot]$ to 100 $[\mathrm{M}_\odot]$
  While this upper limit is realistic, it is also at the lower end of the expected upper limit and could be increased up to at least 120 $[\mathrm{M}_\odot]$ [19]. Since the detectability of low mass stars is of particular interest, the lower limit has been set as low as the method of converting mass to apparent magnitude allows, which is dictated by the Pickles catalogue [46]. For more information see subsection 3.2.1

- (C) Output: 3
  The resulting mass, position and velocity for each star is written into a file.

2.5.2 Snapshots

Figure 2.10 depicts a $10\,\mathrm{kM}_\odot$ cluster near the GC. Stars outside the COV have been removed after the integration in preparation for FITS image creation. As a result the density along the x axis is slightly elongated compared to the y axis since the x axis is parallel to the line of sight.
With a FOV angle of 45° and an unusual location of the observer Figure 2.11 displays FS sampled at the GC. These parameters were chosen to test the code for this extreme case but also because FS of a realistic simulation cannot be nicely represented in a 3D plot.

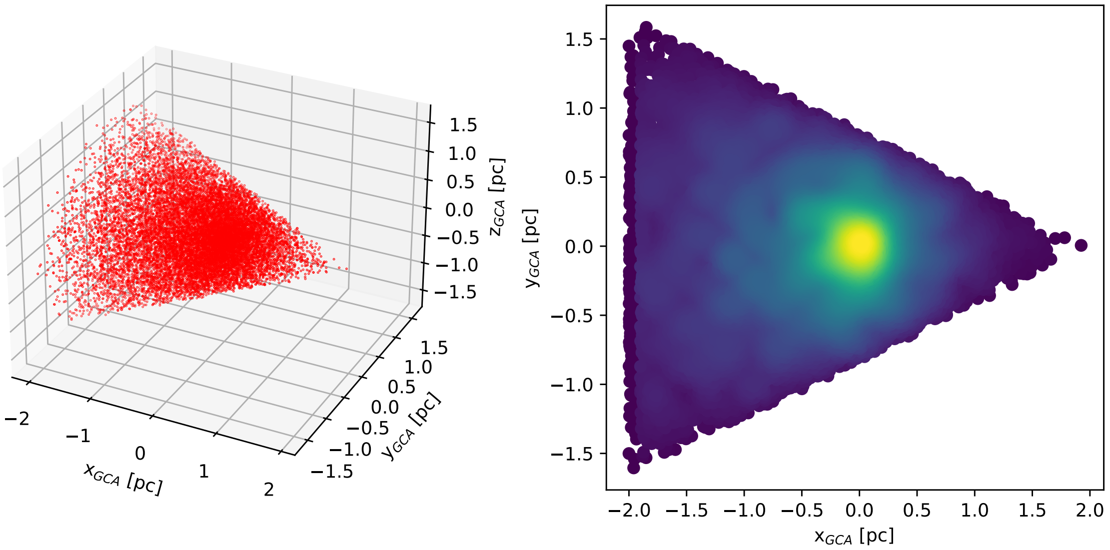

Figure 2.11: Left: A point cloud of the field stars with a mass of $47\,\mathrm{kM_{\odot}}$ which includes the galactic centre at (x, y)=(0,0). Right: projection of the points onto the xy-plane colored by point density.

2.6 Summary of Part I

Masses, positions and velocities of cluster and FSs are generated within the volume of a cone representing the space visible with the ELT and stored in a database. With each timestep all of these positions and velocities are updated. Every set amount of timesteps the data is stored in the database. FSs are only influenced by the galactic potential but CSs influence each other. Hence, the Barnes–Hut algorithm has been implemented to allow for the internal motions of reasonably large clusters to be simulated with limited hardware. Many parameters can be set by the user such as position of the observer, view angle, view distance, location of the cluster, time step size and amount of time steps between observations.
Table 2.2 displays aggregate data for all five fields of view, where $\bar{v}$ is the average velocity and σ_v is the velocity dispersion. σ_v for CS is omitted as it is not correlated with the cluster location. However, it is directly correlated with the cluster mass and ranges from $1.35\,\mathrm{km\,s^{-1}}$ to $6.32\,\mathrm{km\,s^{-1}}$.

Chapter 3

Observing The Milky Way Galaxy

The goal of this part is to turn the simulated data into images observed by the ELT. The main part of this task is done by ScopeSim [37], a package written in Python that creates images in FITS format from given star coordinates and spectra. These coordinates are relative to the observer, whereas so far they have been simulated relative to the centre of the Milky Way. The spectra are based on mass, age, metallicity and distance from the observer.
The content of these images are star clusters of different masses at different positions in the Milky Way. These will ultimately be used to investigate the influence of the field star density and velocity on the detectability and the reliability of cluster membership determination for the cluster stars in different mass ranges.

3.1 Coordinate Systems

In the simulated cluster models, locations and velocities of stars are stored in galactocentric cartesian coordinates (GCA). However, the observer/ScopeSim expect heliocentric equatorial polar coordinates. Moreover, observational data is usually given in heliocentric galactic polar coordinates. This data is used for initial cluster positions within the Milky Way model and to compare results. The implementation of transformations is therefore inevitable. The code has been adapted from GalPot [40].

3.1.1 Galactocentric Cartesian (GCA)

GCA is a right-handed coordinate system with the galactic center in its origin. The projection of the unit-vector $\hat{e}_x$ onto the galactic equator (or midplane) points to the initial location of the sun and $\hat{e}_z$ towards the galactic north pole. Therefore, the direction of galactic rotation at the location of the sun is the negative y axis.

3.1.2 Galactocentric Polar (GCP)

GCP is a spherical coordinate system and similar to GCA. The GC is at the origin O. A point P in GCP is described by its distance ρ to the the GC, the angle θ between the line segment OP and $\hat{e}_{z,GCA}$ and the angle φ between $-\hat{e}_{x,GCA}$ and the projection of OP onto the midplane.
Position and velocity transformation between the two systems goes as follows.

$$\rho = \sqrt{x^2 + y^2 + z^2} \tag{3.1}$$

$$\theta = \mathrm{atan2}(y, x) \tag{3.2}$$

$$\varphi = \arcsin\left(\frac{z}{\sqrt{x^2 + y^2 + z^2}}\right) \tag{3.3}$$

$$\dot{\rho} = \frac{x\dot{x} + y\dot{y} + z\dot{z}}{\sqrt{x^2 + y^2 + z^2}} \tag{3.4}$$

$$\dot{\theta} = \frac{\dot{x}y - x\dot{y}}{x^2 + y^2} \tag{3.5}$$

$$\dot{\varphi} = \frac{z(x\dot{x} + y\dot{y}) - \dot{z}(x^2 + y^2)}{(x^2 + y^2 + z^2)\sqrt{x^2 + y^2}} \tag{3.6}$$

3.1.3 Local Standard of Rest (LSR)

Like GCA, LSR is a right-handed coordinate system. The origin of positions is the location of the sun and the origin of velocity is the velocity of a star on a circular orbit with mean velocity of stars in the solar neighborhood. $\hat{e}_x$ points towards the galactic center, $\hat{e}_y$ towards the direction of galactic rotation and $\hat{e}_z$ approximately towards the galactic north pole.
The location of the sun is given by ([41], [7]):

$$\vec{x}_{sun,GCA} \cong (8.20, 0, 0.014)\text{kpc} \tag{3.7}$$

and the mean velocity [41]

$$\vec{v}_{mean,GCA} \cong (0, -232.8, 0)\text{km/s} \tag{3.8}$$

Since the sun is generally not in the galactic midplane, there is an angle between the planes spanned by $(x, y)_{GCA}$ and $(x, y)_{LSR}$. This angle can be expressed as

$$\sin(\alpha) = \frac{z_{sun,GCA}}{\sqrt{x^2 + z^2}} \tag{3.9}$$

$$\cos(\alpha) = \frac{x_{sun,GCA}}{\sqrt{x^2 + z^2}} \tag{3.10}$$

The transformation of position and velocity vectors from GCA to LSR has to contain a rotation by $-\alpha$ about the y axis.

$$x_{LSR} = \cos(\alpha)(x_{sun,GCA} - x_{GCA}) - \sin(\alpha)(z_{GCA} - z_{sun,GCA}) \tag{3.11}$$

$$y_{LSR} = -y_{GCA} \tag{3.12}$$

$$z_{LSR} = \sin(\alpha)(x_{sun,GCA} - x_{GCA}) + \cos(\alpha)(z_{GCA} - z_{sun,GCA}) \tag{3.13}$$

$$u_{LSR} = -\cos(\alpha)u_{GCA} - \sin(\alpha)w_{GCA} \tag{3.14}$$

$$v_{LSR} = v_{sun,GCA} - v_{GCA} \tag{3.15}$$

$$w_{LSR} = -\sin(\alpha)u_{GCA} + \cos(\alpha)w_{GCA} \tag{3.16}$$

3.1.4 Heliocentric Cartesian (HCA)

The only distinction between HCA and LSR is the origin of the velocity. In HCA the origin is the velocity of the sun. The difference between the average velocity in the solar neighborhood and the sun itself, also called the peculiar motion of the sun, is given by [56]:

$$\vec{v}_{sun,LSR} \cong (11.1, 12.24, 7.25)\text{km/s} \tag{3.17}$$

Transformation from LSR to HCA can be written as:

$$\vec{x}_{HCA} = \vec{x}_{LSR} \tag{3.18}$$

$$\vec{v}_{HCA} = \vec{v}_{LSR} - \vec{v}_{sun,LSR} \tag{3.19}$$

3.1.5 Heliocentric Galactic Polar (HGP)

HGP is a spherical coordinate system with origins for position and velocity identical to those defined in HCA. Coordinates given in this system are often called galactic coordinates. The galactic longitude l is the angular distance in the galactic midplane with $l = 0°$ towards the galactic center. The galactic latitude b denotes the angle below and above the galactic midplane ranging from $-90°$ to $90°$ and r the radial distance.
The transformation from HCA to HGP is identical to the transformation from GCA to GCP (3.1) with $l \equiv \varphi$, $b \equiv \theta$ and $\rho \equiv r$

3.1.6 Heliocentric Equatorial Polar (HEQ)

The following positions and the transformation between HGP and HEQ are described in [13] (p. 1044-1047), the transformation between different epochs in [57] (p 95-105). The latter is dated. The international celestial reference system (ICRS) should be preferred if highest possible accuracy is of concern.
HEQ, like HGP, is a spherical coordinate system having the same origins for position and velocity. However, angles are given in, and normal to, the celestial equator which is not parallel to the galactic midplane. The right ascension (a) is the angular distance in the equator with $a = 0°$ towards the northward equinox. The equinox is the intersection of the ecliptic - the plane in which the earth orbits the sun - and the celestial equator. The declination (d) is the angular distance above or below in the equator.
Since the ecliptic and the equator are in motion, a reference frame is needed. A reference frame consists of quantities defining the coordinate system at a specific time as well as methods to calculate those quantities for any other date. A commonly used reference frame is defined for the J2000.0 epoch (ϵ_0).
In order to transform between HCA and HEQ at ϵ_0, the direction of the north Galactic pole (NGP) and the galactic center (GC) are needed in both basis.
In HCA the NGP is simply $\vec{x}_{NGP,HCA} = (0, 0, 1)$. In HGP, since the direction is normal to the fundamental plane, $b = 90°_{GC,HGP}$. In HEQ at ϵ_0 the direction is

$$\begin{aligned} a_{NGP} &= 12^h 51^m 26.28^s \\ d_{NGP} &= 27°7'41.7'' \end{aligned} \tag{3.20}$$

The GC defines the x axis of HCA: $\vec{x}_{GC,HCA} = (1, 0, 0)$. In GC the same direction is

$$\begin{aligned} a_{GC,HEQ} &= 17^h 45^m 40.0409^s \\ d_{GC,HEQ} &= -29°0'28.118'' \end{aligned} \tag{3.21}$$

To express these basis vectors in HCA basis, they can to be transformed as follows

$$x_{HCA} = \cos(d)\cos(a) \tag{3.22}$$

$$y_{HCA} = \cos(d)\sin(a) \tag{3.23}$$

$$z_{HCA} = \sin(d) \tag{3.24}$$

The third basis vector is the cross product of $\vec{x}_{NGP}$ and $\vec{x}_{GC}$. With these basis vectors the change of basis matrix is

$$M = [\hat{e}_x, \hat{e}_y, \hat{e}_z] \tag{3.25}$$

The full transformation from HCA to HEQ consists of the two steps: the multiplication with M followed by the transformation from Cartesian to spherical as given in (3.1).

For the transformation between HGP and HEQ the direction of the north celestial pole (NCP) is required. NCP is perpendicular to the celestial equator, hence $d_{NGP} = 90°$. In HGP at ϵ_0, NCP is

$$\begin{aligned} l_{NCP} &= 123°55'55.2'' \\ b_{NCP} &= 27°7'41.7'' \end{aligned} \tag{3.26}$$

Using NGP and NCP the transformation from HGP to HEQ at ϵ_0 is

$$\sin(d) = \sin(d_{NGP})\sin(b) + \cos(d_{NGP})\cos(b)\cos(l_{NCP} - l) \tag{3.27}$$

$$\cos(d)\sin(a - a_{NGP}) = \cos(b)\sin(l_{NCP} - l) \tag{3.28}$$

$$\cos(d)\cos(a - a_{NGP}) = \cos(d_{NGP})\sin(b) - sin(d_{NGP})\cos(b)\cos(l_{NGP} - l) \tag{3.29}$$

Three angles, z, θ, ξ describing the precession of both planes are needed in order to transform between epochs ϵ_F and ϵ_D.

$$z = (2306.2181 + 1.39656T - 0.000139T^2)t + (1.09468 + 0.000066T)t^2 + 0.018203t^3 \tag{3.30}$$

$$\theta = (2004.3109 - 0.85330T - 0.000217T^2)t + (-0.42665 - 0.000217T)t^2 - 0.041833t^3 \tag{3.31}$$

$$\xi = (2306.2181 + 1.39656T - 0.000139T^2)t + (0.30188 - 0.000344T)t^2 + 0.017998t^3 \tag{3.32}$$

where t and T are time differences given in units of Julian century.

$$T = \frac{JD(\epsilon_F) - JD(\epsilon_0)}{36525} \tag{3.33}$$

$$t = \frac{JD(\epsilon_D) - JD(\epsilon_F)}{36525} \tag{3.34}$$

With these three rotations, a precession matrix P as well as its inverse can be formalized.

$$P(\epsilon_F, \epsilon_D) = \begin{bmatrix} cz \cdot c\theta \cdot c\xi - sz \cdot s\xi & -cz \cdot c\theta \cdot s\xi - sz \cdot c\xi & -cz \cdot s\theta \\ sz \cdot c\theta \cdot c\xi + cz \cdot s\xi & -sz \cdot c\theta \cdot s\xi + cz \cdot c\xi & -sz \cdot s\theta \\ s\theta \cdot c\xi & -s\theta \cdot s\xi & c\theta \end{bmatrix} \tag{3.35}$$

where $cz = \cos(z)$, $sz = \sin(z)$, $c\theta = \cos(\theta)$, $s\theta = \sin(\theta)$, $c\xi = \cos(\xi)$ and $s\xi = \sin(\xi)$.
Before multiplication with P, the target vector has to be expressed in Cartesian coordinates.

3.1.7 Heliocentric Telescope Polar (HTP)

This coordinate system aims to describe positions as they are observed with a telescope. As with HEQ the right ascension a describes the angular distance in and the declination d the angular distance below and above the midplane. The origin, however is defined by the line of sight vector, that is $\hat{v}_{los} = [r, a, d] = [1, 0, 0]_{HTP}$. Hence one image, taken with a telescope, is a circle in the ad-plane.
It may seem as if the transformation from HGP to HTP and vice versa simply consists of a shift by $\hat{v}_{los}$ in HGP basis. However for any line of sight vector with $b \neq 0$, the result would be an ellipse rather than a circle. Casually speaking, the cone of vision in any spherical coordinate system is a circle when projected onto the unit sphere. While this circle always covers the same range in b, the range in l depends on the distance (b) between the circle and the midplane. With increasing absolute value of b the circles around the unit sphere described by l decrease in size.
While there may be a solution for this issue, a different transformation was devised. Positions can be transformed from HCA to HTP by aligning $\hat{v}_{los}$ with the x axis $\hat{x}$ using a rotation matrix generated as described in (2.46) with the rotation axis defined by $[1, 0, 0]_{HCA}$ and $\hat{v}_{los,HCA}$ Subsequent transformation from Cartesian to polar coordinates as described in the section GCP above completes the transformation.

3.2 Mock Observations with ScopeSim

Images of stars are generated using ScopeSim [37] with the MICADO_Sci instrument, the ELT telescope and the Armazones location package. Parameters differing from default values are:

1. SIM.sub_pixel.flag - Initial tests indicated the necessity of integrating sub pixel shifts
2. DET.width and DET.height - Width and height of the detector plane in pix are set ensuring the image contains the whole COV. The pixel scale of MICADO is 0.004 acrseconds per pixel
3. OBS.dit - The exposure time is adjusted to one hour.
4. scao_const_psf.convolve_mode = "same" - an internal scipy parameter to avoid increasing the simulated field of view outside the limits set by the detector
5. scao_const_psf.rotational_blur_angle - to reflect the rotation of the point spread function (PSF) occurring during one hour, this angle is set to 15 degrees. However, with the approach discussed in section 3.3.1 this will have little to no impact on the results.

For each simulation two images, one for $t = 0$ and one for $t = dt$, are stored as FITS files.

3.2.1 Creating Source Objects

ScopeSim requires one source object for each simulated star. Source objects contain spatial and spectral information. The spatial information consists of x and y in arcsec relative to the FOV axis, here generated by a chain of transformations from GCA to HTP and stored in the appropriate database table.

The spectral information is acquired using multiple functions from the ScopeSim Templates library involving the following steps:

1. The spectral type of a star is determined by looking up the closest spectral type from the Mamajek stellar spectral type look-up table [45] given its mass.
2. The spectrum is taken from Pickles catalogue [46] requiring metallicity in range 0.5 - 2 solar and age of about 5 Gyr.
3. That spectrum is scaled such that it has 0 apparent Vega mag in the V filter.
4. The absolute magnitude M_V of the star in the V filter is determined from its mass using [45] with linear interpolation.
5. The apparent magnitude m_V is obtained from $m_V = M_V + 5\log_{10}(d) - 5$
6. The interstellar extinction e is taken into account using [39]
7. The weight w of the spectrum s is used by ScopeSim to scale the final star photon flux, F

$$F(x, y) = s \times w \tag{3.36}$$

w is calculated calculated from the above quantities thusly:

$$w = \frac{F}{F_0} = 10^{0.4(m_0-(m_V+e))} = 10^{-0.4(m_V+e)} \tag{3.37}$$

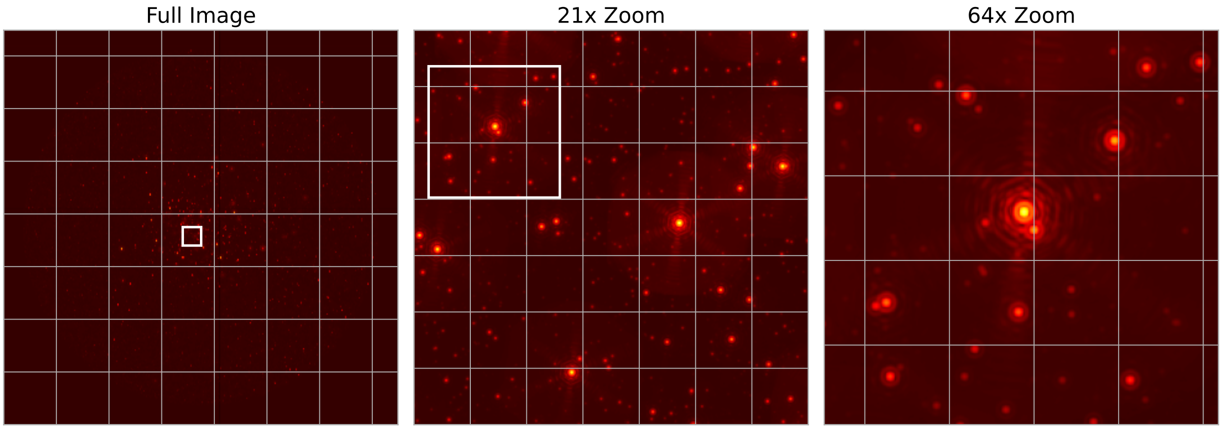

Figure 3.1: Image of a $10\,\mathrm{kM}_\odot$ star cluster and field stars near the GC. The field of view represented in each panel is: 4“ (left), 0.2“ (middle), 0.064“ (right). For context, the current Seeing limit of non-adaptive optic driven telescopes is 0.5“. Without the adaptive optics systems on the ELT, atmospheric turbulence would blur all stars in the middle and right panels into a single blob.

3.2.2 Snapshots

The generated images as displayed in Figure 3.1 already show some upcoming difficulties. Diffraction spikes of bright stars obscure nearby stars with lower luminosity. Worse, these artifacts are sometimes indistinguishable from real stars. Figure 3.2 displays a star cluster of identical mass but opposite direction for comparison.

3.3 Data Reduction with Photutils

With the help of Photutils [11] the 2D HTP positions and fluxes of stars are detected from the FITS files generated during observation. In a first step, all stars are stored in the database, each having exactly one location corresponding to the timestep of the FITS file.
The following method, while yielding decent results, is certainly not optimal. Due to hardware and time constraints, options such as Image Segmentation were not feasible. Moreover, the parameters of the chosen method were not optimized beyond some spot checks.

3.3.1 Detecting Stars

Background

Testing FITS files generated with no input sources still yield some amount of detected sources. With the parameters described in subsection 2.5.1 used for the 25 simulations, 125 sources were detected against an empty background. The FITS files contain a raster of 64 images, sometimes overlapping and sometimes separated by one pixel due to rounding. This leads to wrong detections at the corners. However, this effect only explains a fraction of the detections.

Masking bright stars

The diffraction spikes and sections of the halos of bright stars due to the ELT’s strongly segmented PSFs were wrongfully detected as stars. Increasing the detection threshold would have meant not detecting real faint stars in different areas. Hence the decision was made to mask square areas around bright stars leading to only one detection within those areas.

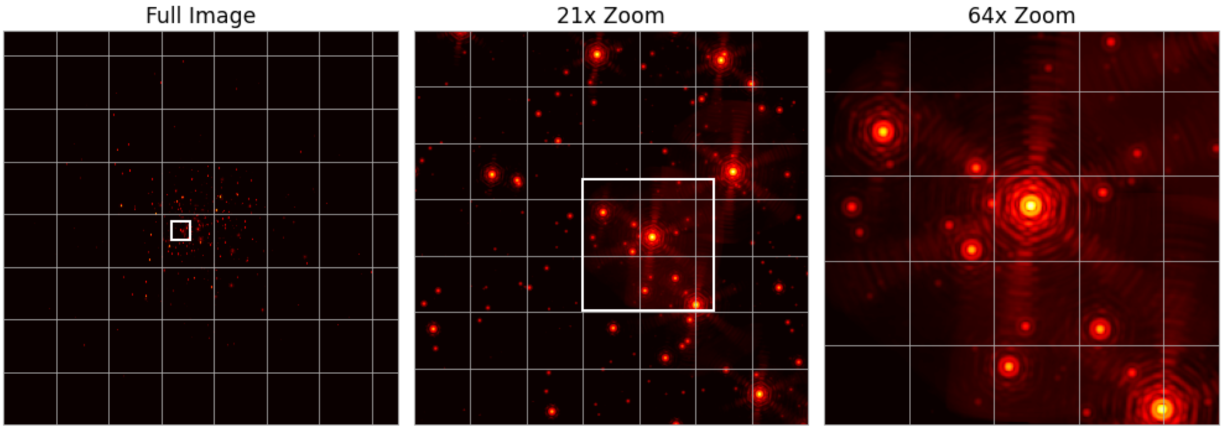

Figure 3.2: Similar to Figure 3.1. Image of a $10\,\mathrm{kM}_\odot$ star cluster and field stars at the galactic anti-centre. The lower ambient background flux due to the vastly lower field star density is apparent when compared to all panels in Figure 3.1. Additionally the optical artefacts of the ELTs segmented PSF are also visible in the diffraction spikes and AO-halos seen around bright stars (right panel).

The side length l_i of the square depends on the flux F_i of the stars: $l_i = f(F_i)$.
To find the appropriate function, FITS image files for single stars at a given distance and with varying mass were generated, the sources in each file detected, using DAOStarFinder, and their flux and maximum distance between the correct and any wrong sources calculated. A linear fit of the resulting dataset Appendix A lead to the "empirical" function

$$l_i = \begin{cases} 0 \text{ if } F_i < 100 \\ 0.01 * F_i + 28 \text{ if } F_i \geqslant 100 \end{cases} \tag{3.38}$$

The DAOStarFinder method is called twice:

1. To find the bright stars and generate the mask. The resulting table contains one row for each source.
   This table is sorted by the flux column in descending order and iterated from top to bottom until the current entry has $F_i < 100$.
   Elements of the mask - a 2D Boolean array with the same size as the image - are updated. All elements inside the box with side length (3.38) are set to true and the current table entry stored in a new table if located outside a masked area.

2. For passing the mask parameter generated in the previous step and returning sources outside the masked areas.

Both the bright sources recorded after the first and the faint sources returned from the second call are stored in the database.

3.3.2 Extracted positions

As indicated in relation to Figure 3.1, diffraction spikes of bright stars are problematic. The star was masked in the consequence that none of the other stars were recognised in its vicinity as can be seen in Figure 3.3. More elaborate algorithms should be developed to improve this process. An alternative method provided by photutils, namely image segmentation, was tested. While the results with smaller test images were promising, the size of the full images reached the limits of

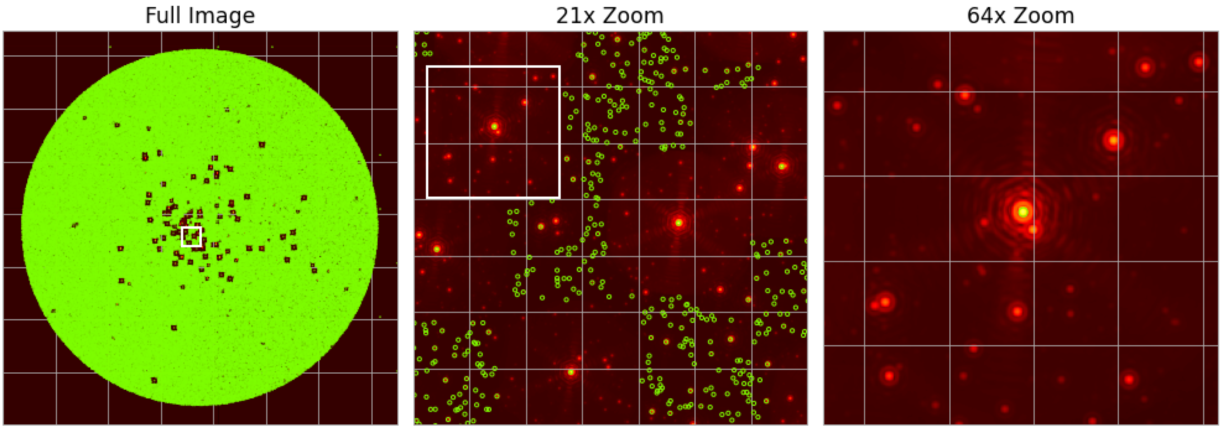

Figure 3.3: 2D HTP positions (green) extracted from an image of a star cluster and field stars near the GC. The zones void of green circles (middle) illustrate how areas around the brightest stars are discarded by the detection algorithm. This is done to avoid false positives resulting from the segmented nature of the PSF diffraction spikes created by the ELT. The field of view represented in each panel is: 4“ (left), 0.2“ (middle), 0.064“ (right).

the hardware available to the author. Splitting the image into sub-sections would be an option to consider.

Comparison of the simulated and extracted star positions displayed in Figure 3.4 makes clear how many stars are not detected, especially in the vicinity of bright stars.

This image is based on a total of 368127 simulated stars and from this image a total of 243657 stars or $\approx 66\,\%$ relative to the simulated stars were extracted.

3.4 Summary of Part II

Positions of CS and FS at two time stamps are transformed from galactocentric cartesian to heliocentric polar coordinates. Masses and distances to the observer are used to calculate the apparent magnitudes while extinction is also taken into account. From this data images are generated using ScopeSim to simulate observation with the ELT.

2D heliocentric polar coordinates of stars and associated fluxes are extracted from these images using photutils and stored in the database.

This concludes the observations. What remains is to analyse the observed data and determine with how much certainty it is possible to determine which stars are cluster stars and which are field stars.

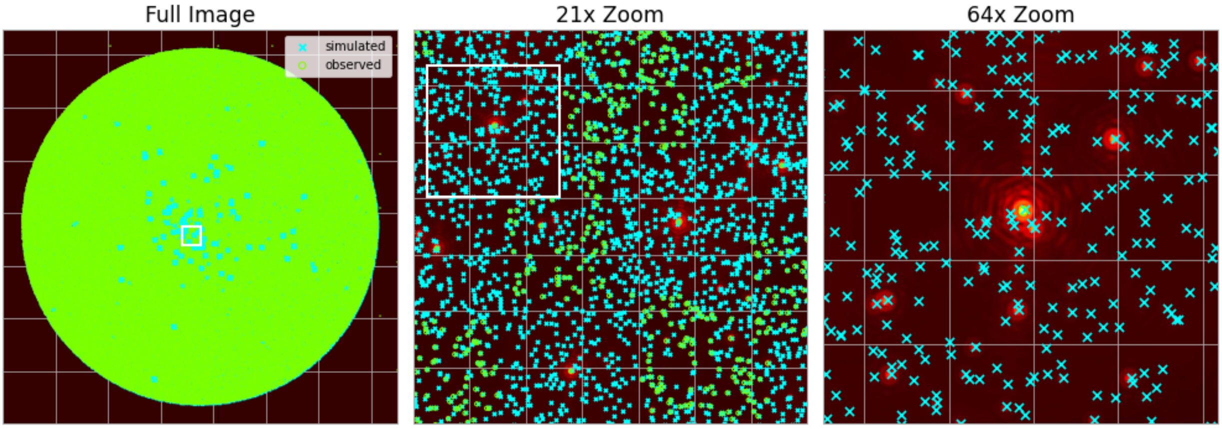

Figure 3.4: Similar to Figure 3.3. Simulated HTP positions marked with cyan crosses and extracted HTP position market with green circles of a star cluster and field stars near the GC. The cyan crosses illustrate the shear number of simulated low mass stars that are undetectable due to the high ambient flux at the galactic centre. The field of view represented in each panel is: 4“ (left), 0.2“ (middle), 0.064“ (right).

Chapter 4

Interpreting The Milky Way Galaxy

After a considerable amount of simulated and observed data has been created, the database has a size of about 13 GB, the goal to determine if and with what accuracy IMFs can be determined close to the GC is within reach.
There is still one essential component missing, and that is to classify the observed stars, to determine whether they are CSs or FSs. For this purpose, a clustering algorithm is used and its performance is determined. This performance can only be determined because the simulated data and thus the correct positions and assignments exist and are known. It defines the certainty with which assignments of stars are correct and can be used as an indicator for future observations.

4.1 Velocity approximation

The proper motion of a star can be approximated from its position at two different timestamps via first order Taylor expansion

$$v_i = \frac{x_i\left(t+dt\right) - x_i\left(t\right)}{dt} \tag{4.1}$$

However, this is only possible if the positions at two different timesteps can be accurately associated with the same star s_i. The assumption that $\vec{x}(t+dt)$ belongs to the same star as $\vec{x}(t)$ if their Euclidian distance is smaller than the distance of $\vec{x}(t)$ to any other $\vec{x}(t+dt)$, only hold true for small dt. However, due to the discreteness of images, dt has to be large enough so that the change in position is detectable between timesteps. The pixel scale - the ratio of arcsec to pixel - dictates a lower bound for dt.
Since the data results from a simulation, it is trivial to verify whether or not the attribution of the two positions is indeed correct. In fact, tests using only the Euclidian distance as a metric with $dt = 1\,\mathrm{d}$ lead to a small but significant amount of wrong assignments.
An additional condition was introduced. Stars at $\vec{x}(t)$ and $\vec{x}(t+dt)$ have to have a similar apparent magnitude m to be considered the same star.

$$\left|1 - \frac{m_i\left(t\right)}{m_j\left(t+dt\right)}\right| < \varepsilon_m \tag{4.2}$$

where ε_m is the maximum relative difference in apparent magnitude. With this constraint, all positions where correctly assigned during further tests when using the exact positions.
Table 4.1 shows the relative number of incorrect assignments during the velocity estimation. It should be noted that the mapping between observed and simulated stars on which these calculations are based is itself subject to error, and that incorrect mappings for field stars are usually irrelevant, since they only distort the results if they happen to be assigned a velocity that identifies them as a cluster star.
As depicted in Figure 4.1 the proper motion of stars is well suited to distinguish between cluster stars and field stars. The position on the other side is so unsuitable that cluster and field stars would hardly be distinguishable in a 2D HTP position plot.

		cluster mass [$\mathrm{kM_\odot}$]				
		0.64	1.60	4.00	10.00	25.00
angle [°]	180	0.6	0.8	1.4	1.2	0.8
	25	0.8	0.9	1.1	1.3	1.7
	10	1.1	1.1	1.2	1.3	2.1
	5	1.5	1.5	1.6	1.9	2.6
	0	3.7	3.7	3.8	3.8	4.1

Table 4.1: Percentage of stars with observationally detected velocities matching the velocity from the star's simulation input data. Even in the densest cluster at the galactic centre the reliability of the detected star velocities is around 96 %

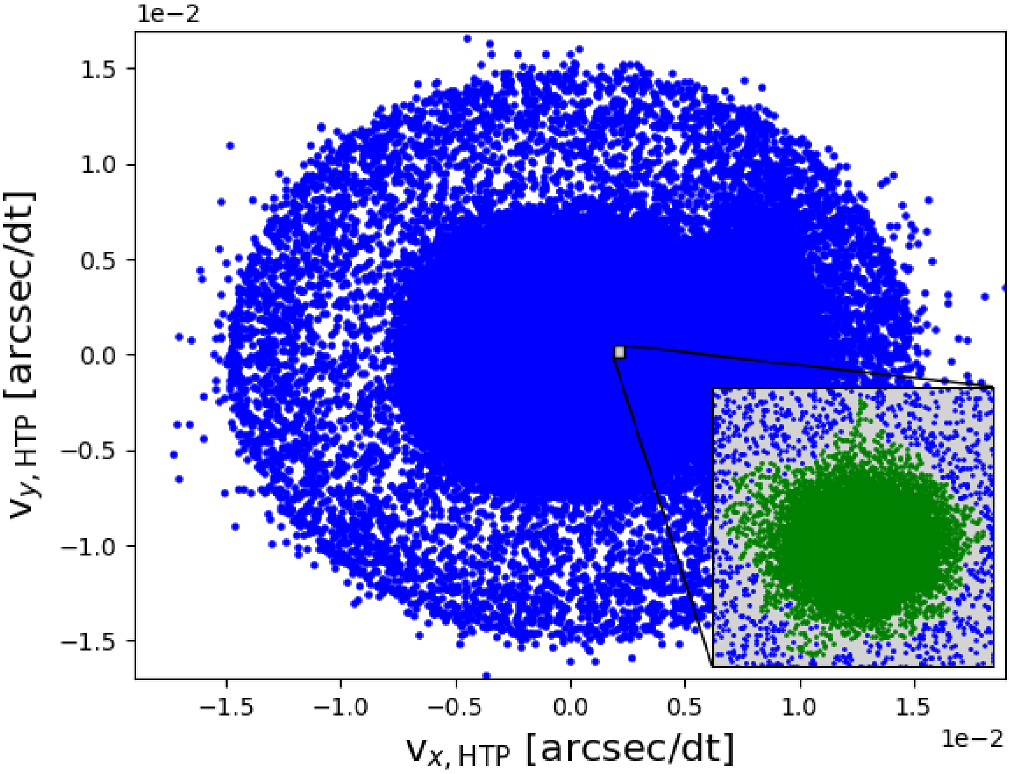

Figure 4.1: 2D HTP velocity approximation for CS (green, inset) of a $1 \times 10^4\,\mathrm{kM_\odot}$ cluster near the GC and FS (blue) along the line of sight. The time between observations (dt) is $28\,\mathrm{d}$. Given the extremely small region of the velocity parameter space occupied by the cluster-stars, cluster membership could be assigned to stars found in this space, based solely on a stars velocity characteristics.

4.2 Cluster Membership Detection

4.2.1 DBSCAN Algorithm

The clustering algorithm of choice is DBSCAN since it is density based and able to detect clusters of arbitrary shape. Additionally and contrary to other algorithms the amount of clusters to find is not a parameter. DBSCAN detects any clusters present in the data based on two parameters:

1. ϵ: the maximum distance between points to be considered neighbors
2. nPoints: the minimum amount of neighbors for a point to be classified as core point.

During execution all data points are classified as one of the following:

1. core point: a point with at least nPoints within ϵ:
2. border point: a point having at least one core point but less than nPoints within ϵ:
3. noise/outlier: any other point

The implementation of DBSCAN can be summarized as follows: Iterate the list of points. If the current point is not already classified, check if it meets the requirements to be classified as core point. Once a core point has been found, the neighboring points of that point are tested. If they too have enough neighbors the recursion continues until all neighbors are classified as either core or border points.

In a naive implementation, the distance of each point to every other point is checked. The time complexity of such an implementation is $O(n^2)$. Moreover, for large datasets the recursion can lead to stack overflow.

R*-tree or similar data structures can be used to improve the performance to an average of $O(n \log n)$ [20]. The library mlpack [15] was used, which includes an implementation of DBSCAN supporting R*-tree and many other trees.

Initially and in addition to the standard condition ϵ_x for the spatial distance between points a supplementary condition ϵ_v was introduced. The difference in velocity between two stars has to be smaller than ϵ_v for them to be classified as neighbors:

$$\|\vec{v}_1 - \vec{v}_2\|_2 < \epsilon_v \tag{4.3}$$

Large ϵ_x lead to more accurate membership detection. It turned out, the spatial distance condition does not benefit the results at all and it was dropped. For larger areas than used here, constraining the spatial distance, for instance via subdivision, should be beneficial.

4.2.2 Parameter optimization

The quality of the cluster analysis with DBSCAN depends on the choice of its parameters. Figure 4.2 depicts the precision for a $1\,\mathrm{kM}_\odot$ cluster $300\,\mathrm{pc}$ from the GC. Decreasing ϵ leads to a higher precission until it is too small, at which point multiple clusters are detected. Based on this observation ϵ was set to $1.1 \cdot 10^{-5}$ and nPoints to 200 for all simulations. Not optimising these parameters would result in more FS being incorrectly classified as CS.

This optimization is only possible because the ground truth set, which consists of the simulated CS and FS, is known. This is arguably an unfair advantage, as this is not normally the case. However, simulations like these can be used for this very reason. Creating a model that is as close as possible to the real observations and determining the parameters based on this model should provide useful parameters for running clustering algorithms on observed data sets.

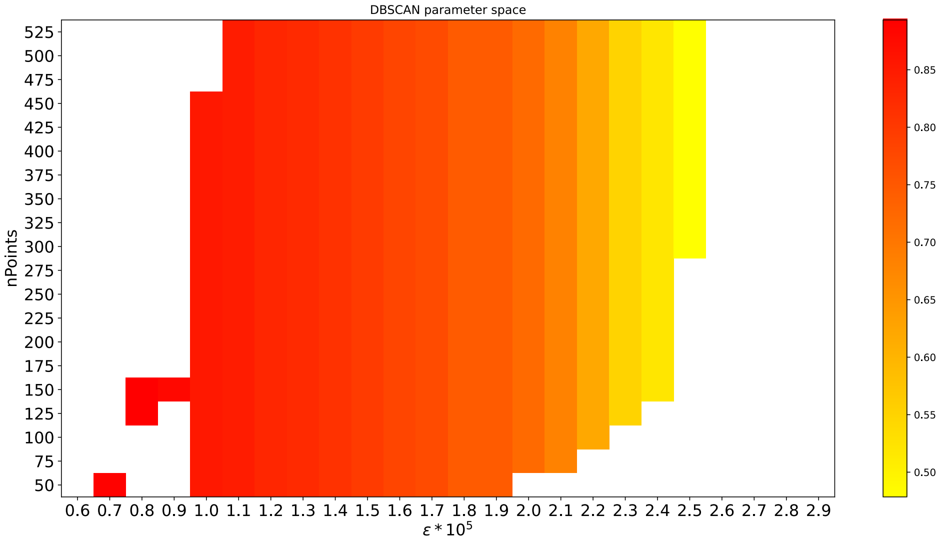

Figure 4.2: Precision of the DBSCAN algorithm for a $1\,\mathrm{kM}_\odot$ cluster $300\,\mathrm{pc}$ from the GC depending on the DBSCAN parameters. In our case, nPoints is the minimum number of stars with a velocity within range ε from each other. Together these parameters can be interpreted as minimum velocity density.

4.3 Membership reliability indicator

Observed stars are mapped to simulated stars via their proximity in order to measure the performance. If a star is not the closest observed star to any simulated star it remains not mapped. Not mapped stars exist due to section 3.3.1 and parts of the PSFs of bright stars being detected as stars. Observed stars can then be attributed one of the following types:

1. True Positive (TP): correctly classified as cluster star.
2. False Positive (FP): wrongly classified as cluster star.
3. True Negative (TN): correctly classified as field star.
4. False Negative (FN): wrongly classified as field star.
5. Unconfirmed Positive (UP): not mapped star classified as cluster star. Treated as FP.
6. Unconfirmed Negative (UN): not mapped star classified as field star. Not taken into account since FN is unlikely.

4.3.1 Accuracy

$$A = \frac{TP + TN}{TP + TN + FP + FN} \tag{4.4}$$

With a large amount of field stars relative to cluster stars, this metric is not ideal as it will give a good rating even if most cluster stars are FN.

4.3.2 Precision and Recall

When FPs are more problematic than FNs, the precision P should be high

$$P = \frac{TP}{TP + FP + UP} \tag{4.5}$$

On the flip side, if FNs are a big concern, but FPs tolerable, the recall R is a good metric

$$R = \frac{TP}{TP + FN} \tag{4.6}$$

4.3.3 F1 Score

This metric is a balance between P and R. Contrary to A TN is not taken into account.

$$F_1 = 2\frac{P \cdot R}{P + R} = \frac{TP}{TP + 0.5(FP + UP + FN)} \tag{4.7}$$

When studying IMFs classifying FSs as CSs is arguably just as problematic as classifying CSs as FSs because both lead to errors in the mass distribution approximated on the basis of the data. The F1 score has a range from 0 to 1. The closer to 1, the more reliable are the results of the classification.

4.3.4 Limitations

Because of the unmapped stars, especially UPs, the indicator will never be exact. However, since UPs are treated like FPs, the indicator is a worst-case estimate in this respect, and the true reliability is probably higher.

The indicator is used to measure the performance of DBSCAN for varying regimes of the cluster mass distribution (high-mass, solar-mass, low-mass stars). Since more massive stars can be classified more reliably, more massive stars within a mass region increase the reliability of that region. A star with $0.1\,\mathrm{M}_\odot$ is less likely to be TP than a star with $0.5\,\mathrm{M}_\odot$.

Most importantly, the indicator is based on data generated by a simulation. Therefore, the indicator is only as realistic as the underlying model.

Chapter 5

Results and discussion

Depending on the total cluster mass the amount of simulated cluster stars (SCSs) ranges from 1.3×10^3 to 40.4×10^3 stars while the amount of mapped cluster stars (MCSs) lies between 1.0×10^3 and 16.4×10^3 stars. The decrease in detectability of CSs is due to increasing CS density and has no direct impact on the clustering performance. The difference between observed stars (OSs) and mapped stars (MSs) is negligible, in fact the absolute amount of not mapped stars decreases with increasing number of SCSs. This is due to the higher simulated stellar density in 2D HTP. Observed stars are assigned to the closest simulated star within a small radius. If there is no simulated star within the radius, they are not mapped.

While the number of simulated field stars (SFSs) remains constant, the number of mapped field stars (MFSs) decreases with increasing number of CSs because bright CSs hide FSs as depicted in Figure 5.1. This inverse relationship does impact the clustering performance to some degree, less MFS means less potential FPs as well as TNs, the latter are not relevant for Precision and F1 score.

Figure 5.2 displays the precision using the velocity of OSs and Figure 5.3 for the velocity of simulated stars (SSs). The only relevant difference between simulated and observed HTP proper motion is the accuracy of position and consequently of velocity. While both figures show the same relationships, the drop in overall performance due to inaccuracies introduced during observation and source detection are painfully apparent. Techniques must therefore be developed to increase the accuracy of star centroiding if the theoretical accuracy limit is to be achieved.

A comparison of Figure 5.4 with Figure 5.2 shows significant deviations. When it comes to determining the IMF of a cluster, the F1 score is more relevant as both FPs and FNs are taken into account. Nevertheless, it is worth paying attention to the precision. As the values here are consistently better, the clustering parameters may have been chosen too strictly. In fact, the parameters were optimised on the basis of the precision. It would be interesting to investigate what changes would occur if the parameters were optimised according to F1.

As is discernable in Figure 5.2 and Figure 5.3 the precision, with one exception, is correlated with the angle. Curiously for the same cluster mass the precision is lower at 10° than at 5°. The same phenomenon, but with a lesser degree of intensity, can be seen in Table 5.1 for the F1 score.

Figure 5.5 provides the explanation for this outlier. At 10° the average field star velocity is closer to the average cluster star velocity than at any other angle, making it harder to differentiate between cluster and noise from the field stars.

The bigger the cluster mass, the higher the cluster star velocity density, which implies the second correlation - precision as well as F1 score with cluster mass - presented in Figure 5.2 and Table 5.1.

Figure 5.6 displays examples for the 2D HTP velocity space of two simulated clusters near the GC. In this example the $0.64\,\mathrm{kM}_\odot$ cluster only has 1143 stars inside the circle while the $10\,\mathrm{kM}_\odot$ cluster has 3158. In both cases statistically the same amount of FSs fall within that area, leading to a higher ratio of FPs and therefore a lower precision for the lower mass cluster.

When studying the low-mass regime of the IMF at large galactic distances ∼8 kpc, due to the

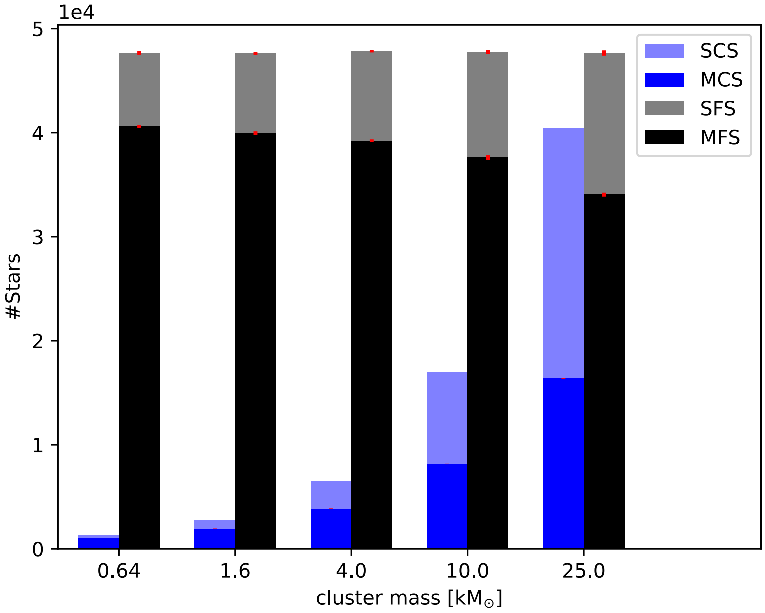

Figure 5.1: Number of simulated (light) versus detected (dark) stars in the cluster (blue) and field (black) populations at a galactic longitude of 10° for different cluster masses. The relative fraction of mapped stars decreases significantly as the 2D HTP star density increases.

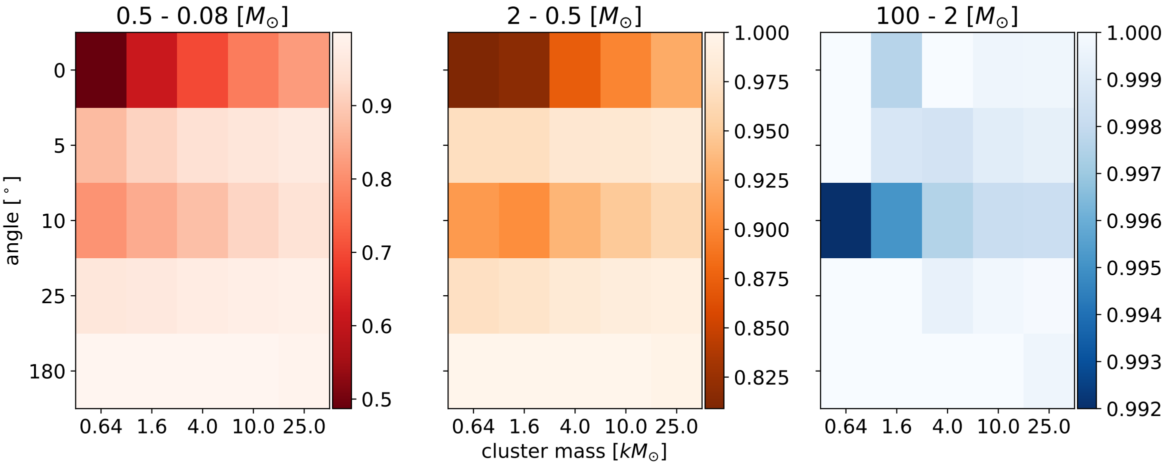

Figure 5.2: Precision - a metric indicating the reliability with which observed cluster stars are actually simulated cluster stars - for different mass bins, angles and cluster masses

Angle °	Mass $\mathrm{kM_\odot}$	% Found	F1 Score
180	0.64	34	0.63
180	1.60	37	0.81
180	4.00	28	0.85
180	10.00	30	0.93
180	25.00	33	0.94
25	0.64	36	0.62
25	1.60	40	0.75
25	4.00	34	0.81
25	10.00	34	0.87
25	25.00	33	0.92
10	0.64	29	0.45
10	1.60	39	0.62
10	4.00	39	0.72
10	10.00	35	0.80
10	25.00	32	0.87
5	0.64	18	0.34
5	1.60	25	0.49
5	4.00	28	0.61
5	10.00	30	0.72
5	25.00	26	0.81
0	0.64	41	0.39
0	1.60	40	0.52
0	4.00	40	0.62
0	10.00	35	0.71
0	25.00	28	0.76

Table 5.1: Mass range: $0.08\,\mathrm{M_\odot}$ to $0.5\,\mathrm{M_\odot}$. Percentage of found cluster stars relative to simulated cluster stars and detection reliability (F1) score for such. Regardless of the angular distance from the galactic centre, on average only $\sim 30\,\%$ of a clusters low mass stars will be detected and attributed membership for clusters at a distance of $8\,\mathrm{kpc}$ from the Earth. Similar tables for the solar- and high-mass ranges are included in the appendix.

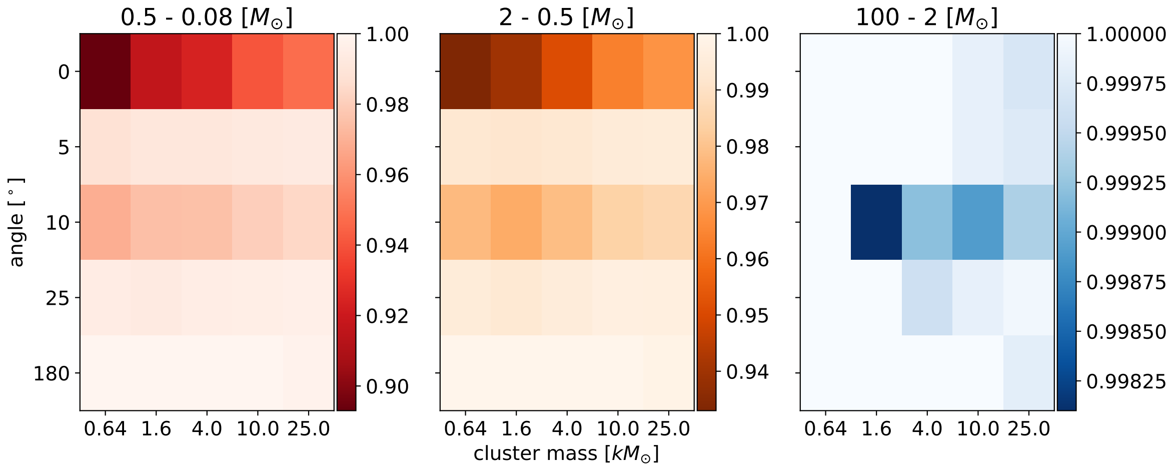

Figure 5.3: Precision using accurate velocities generated by using the simulated rather than the observed positions. This represents an ideal world where the telescope has close to infinite resolution and image extraction is possible without error. This figure illustrates how important it is to be able to make accurate position measurements.

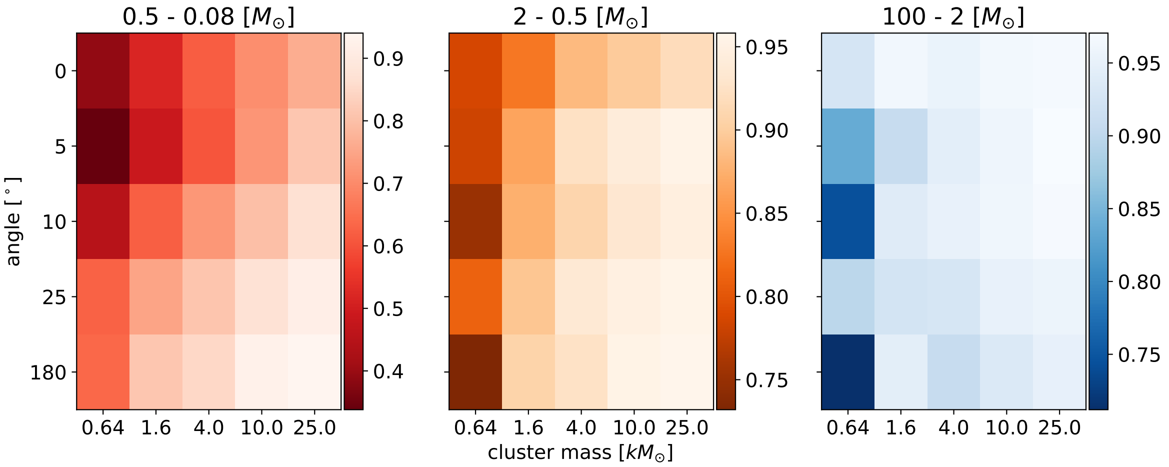

Figure 5.4: F1 score for different mass bins, angles and cluster masses. This is the measure of the reliability of the determination of cluster membership. A high F1 score is a mandatory prerequisite for IMF studies based on the classified set of detected stars.

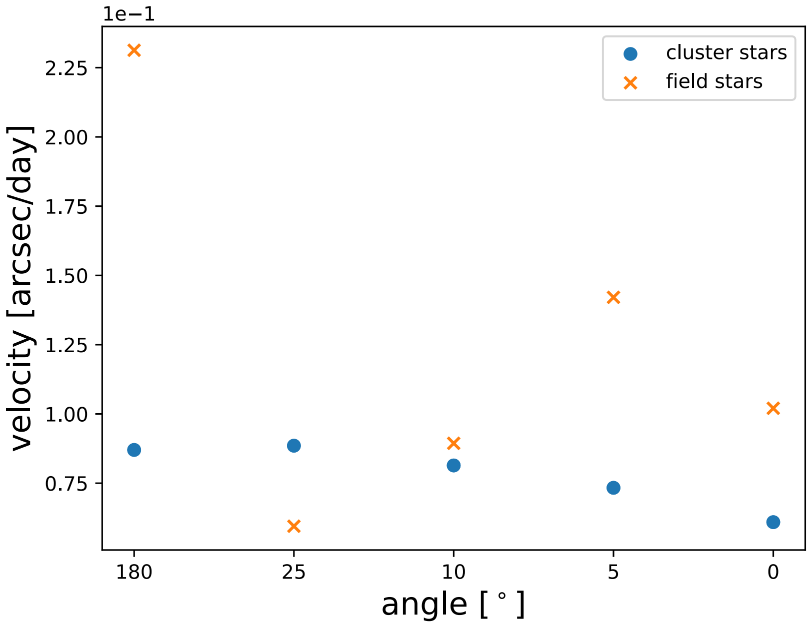

Figure 5.5: Average cluster and field star velocity at different angles. The clustering algorithm performs relatively poorly at galactic longitudes around 10° for cluster at a distance of 8 kpc. This is due to the average velocity of field stars being very similar to the circular velocity at this position in the galaxy.

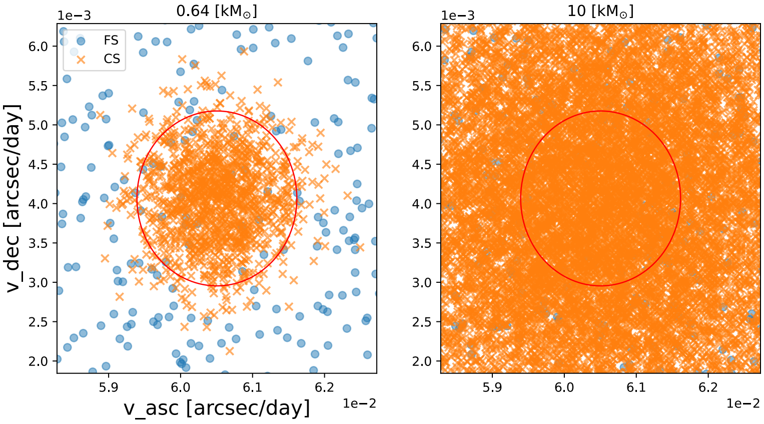

Figure 5.6: 2D HTP velocity of simulated clusters. The higher relative FS density in case of the $0.64\,\mathrm{kM_\odot}$ cluster (left) leads to a lower membership precision when compared to the $10\,\mathrm{kM_\odot}$ cluster (right).

direct correlation between the reliability of classification of stars and cluster mass, the cluster should be massive indeed. This is especially true near the GC. In addition, the mass range dependent detection rate has to be taken into account (Table 5.1), since only $\sim 30\,\%$ of the stars in the mass range $0.08\,\mathrm{M_\odot}$ to $0.5\,\mathrm{M_\odot}$ are detected.

Chapter 6

Conclusions

The primary goal of this project was to determine how reliable the cluster membership data obtained with the ELT will be for future studies of the initial mass function in distant young star clusters, for example at the galactic centre.
To achieve this goal a piece of software has been created to model the Milky Way potential as well as observable distribution of stars in the Milky Way. The software has been utilized to observe scenes for various parts of the Milky Way. Young stellar clusters, ranging in mass from $640\,\mathrm{M}_\odot$ to $25\,000\,\mathrm{M}_\odot$, were added to each of these scenes in order to mimic the observational conditions that are to be expected with the ELT. The software could be used as a background for future observation simulations with, but not limited to, ScopeSim.
These scenes were converted to images, the astrometric velocity data of all detected stars extracted from these images, cluster analysis performed on this data, and the performance of the clustering algorithm measured to show which mass ranges will be reliably available to future studies of the IMF with the ELT. A star cluster membership reliability indicator for the three main sections of the IMF for each of the cases (from massive/tiny clusters in the galactic centre to tiny/massive clusters at the galactic anti-centre) has been determined.

According to this indicator, the reliability of cluster membership determinations in the galactic centre is restricted to masses $>0.5\,\mathrm{M}_\odot$ for low mass ($<1\times10^4\,\mathrm{M}_\odot$) clusters, but potentially acceptable in all studied mass regimes including $0.5\,\mathrm{M}_\odot$ to $0.08\,\mathrm{M}_\odot$ for truly massive (e.g. $>1\times10^4\,\mathrm{M}_\odot$) clusters. Outside of the GC, the full IMF was available in all simulated young star clusters out to $8\,\mathrm{kpc}$.

The results presented, particularly Figure 5.2 and Table 5.1, indicate that data gathered with the ELT will indeed be accurate enough to study the high- and solar-mass regions of the IMFs in YMCs near the GC. However, it remains questionable if this is still the case for stars with masses less than $0.08\,\mathrm{M}_\odot$. Information about this mass regime is sparse. There is no generally accepted IMF for the MW stars covering this mass regime. Furthermore, Pickles catalogue [46] does not contain spectra below M9, while these stars would have spectral type L or even T. Moreover, the membership attribution precision obtained for clusters in the galactic centre in the mass range $0.5\,\mathrm{M}_\odot$ to $0.08\,\mathrm{M}_\odot$ is already quite low. That is not to say it will not be possible to study the low mass range of the IMF in the crowded environment of the galactic centre, but that improved astrometric and star detection techniques should be developed to address this challenging task.

For any future works that are based on the results presented here, the following implementation improvements are recommended:

1. A more accurate bulge model, for example [63]
2. Additional observation epoch snapshots to recover temporarily hidden stars and get a more accurate velocity estimation.

3. A sophisticated method for extracting positional data like point spread function fitting.
4. Accurate determination of the ideal time step size based on cluster location and kinematics.

The code, including some inline documentation, and a link to an external documentation is publicly available on GitHub in the form of two visual studio solutions. `N_Body.sln` contains a C++ project and implements the simulation and cluster analysis while `Photometry.sln` is a collection of python scripts used for image generation and extraction. The data, small enough to be hosted on GiHub, can be found here.

Finally, a word of advice to students: Make sure you know what you are getting into. As wonderful and exciting as a project may sound, ask yourself if it is doable in a reasonable time frame and do not fall into delusions of grandeur.

Appendix A

Appendix

flux	box_size	dist	mass
927146.1955	254.3559872	127.1779936	10
890635.019	254.3417547	127.1708773	9.9
857036.8725	254.341936	127.170968	9.8
823955.0858	254.3421943	127.1710971	9.7
793135.9042	254.3424033	127.1712017	9.6
762592.0798	254.3426546	127.1713273	9.5
734504.8423	254.3429091	127.1714545	9.4
707751.1254	254.3431486	127.1715743	9.3
681256.1109	254.3434061	127.1717031	9.2
656346.0444	254.3436538	127.1718269	9.1
633104.9017	254.3439632	127.1719816	9
609936.5628	254.3442026	127.1721013	8.9
587640.2069	254.3445212	127.1722606	8.8
566233.046	254.3448084	127.1724042	8.7
545639.6678	254.3451645	127.1725822	8.6
525443.3219	254.3454953	127.1727477	8.5
506252.3011	254.4948138	127.2474069	8.4
487489.4659	254.3462375	127.1731188	8.3
470008.9293	254.3465892	127.1732946	8.2
462754.3324	254.3470858	127.1735429	8.1
445797.2677	254.5130792	127.2565396	8
429456.9678	254.347868	127.173934	7.9
413760.4129	254.3482648	127.1741324	7.8
398652.2024	254.3487825	127.1743912	7.7
384123.4617	254.4173555	127.2086778	7.6
370111.5523	253.8093122	126.9046561	7.5
356487.63	254.4810594	127.2405297	7.4
343530.5029	255.0658948	127.5329474	7.3
316316.5998	247.8349505	123.9174752	7.2
309163.7247	254.4288941	127.2144471	7.1
302130.3778	254.4303415	127.2151707	7
295295.4188	254.5012123	127.2506062	6.9
288627.7467	254.433333	127.2166665	6.8
282129.2052	254.4345462	127.2172731	6.7
275630.1016	254.436262	127.218131	6.6
269416.7466	254.4377591	127.2188795	6.5

263376.811	247.9665145	123.9832573	6.4
257390.5638	247.9972751	123.9986376	6.3
251577.0397	252.6213071	126.3106536	6.2
245854.0065	248.0135846	124.0067923	6.1
236400.0465	248.0575239	124.0287619	6
227300.7517	252.618173	126.3090865	5.9
218570.2985	252.6201478	126.3100739	5.8
210129.5831	247.9292325	123.9646163	5.7
202041.5421	247.85708	123.92854	5.6
194255.2774	252.6363119	126.318156	5.5
186750.9496	252.6021078	126.3010539	5.4
182535.794	247.9673489	123.9836745	5.3
178401.698	248.0481722	124.0240861	5.2
174325.8134	252.6377075	126.3188537	5.1
170400.5422	252.6334207	126.3167103	5
248519.9168	247.7858731	123.8929365	4.9
242908.6771	247.9706455	123.9853228	4.8
237403.2487	248.0166034	124.0083017	4.7
232060.6523	247.9419667	123.9709833	4.6
218259.9677	254.6442946	127.3221473	4.5
205273.3003	247.9794943	123.9897472	4.4
193150.6701	250.4719141	125.2359571	4.3
181724.6168	252.6310455	126.3155227	4.2
170942.9686	252.6333644	126.3166822	4.1
160789.262	252.6181038	126.3090519	4
168811.5177	247.8041635	123.9020817	3.9
162697.5008	252.6385607	126.3192803	3.8
156860.6692	252.6179306	126.3089653	3.7
151196.1118	247.8991699	123.949585	3.6
145724.8797	248.360639	124.1803195	3.5
150293.5107	248.072207	124.0361035	3.4
130973.0674	255.4786549	127.7393274	3.3
114105.3359	252.5656424	126.2828212	3.2
99358.44939	248.5393443	124.2696721	3.1
86537.23392	251.6269223	125.8134612	3
75357.58044	251.6432071	125.8216036	2.9
65650.99523	251.6614012	125.8307006	2.8
63683.16206	251.6658441	125.8329221	2.7
61750.32575	251.67074	125.83537	2.6
59884.23739	252.6195792	126.3097896	2.5
57772.09156	251.6814637	125.8407319	2.4
50097.62697	253.4222927	126.7111463	2.3
43479.65427	216.2939201	108.14696	2.2
33899.676	248.6107083	124.3053542	2.1
29960.07512	248.6307907	124.3153953	2
24613.56833	150.7541002	75.37705012	1.9
36933.09895	198.6613702	99.3306851	1.8
29129.77414	199.0091892	99.50459462	1.7
27120.64332	216.4733782	108.2366891	1.6
20229.98476	170.1296746	85.06483729	1.5

19179.36077	179.7883487	89.89417436	1.4
15120.70563	151.6853158	75.84265791	1.3
11210.70479	86.37067622	43.18533811	1.2
7990.562518	62.34638126	31.17319063	1.1
6367.416643	103.8925506	51.94627529	1
4117.980781	51.12273987	25.56136994	0.9
3939.712223	52.55001005	26.27500503	0.8
2698.416769	51.4333436	25.7166718	0.7
1046.477108	27.12953968	13.56476984	0.6
727.6929275	27.40087693	13.70043846	0.5
537.6169065	21.17919258	10.58959629	0.4
201.0127308	20.96270907	10.48135453	0.3
96.41247775	0	0	0.2
26.95062209	0	0	0.1

Table A.1: Dataset for "empirical" mask function. The mask function hides stars within a range of a bright star from detection during data extraction using photutils. Since this function was developed by the author, the raw data is included here so that the reader can check the validity of the function.

Angle °	Mass $\mathrm{kM_\odot}$	% Found	F1 Score
180	0.64	41	0.73
180	1.60	49	0.91
180	4.00	35	0.92
180	10.00	34	0.95
180	25.00	40	0.96
25	0.64	61	0.81
25	1.60	58	0.89
25	4.00	49	0.94
25	10.00	45	0.95
25	25.00	43	0.95
10	0.64	61	0.75
10	1.60	73	0.87
10	4.00	63	0.91
10	10.00	52	0.93
10	25.00	47	0.95
5	0.64	61	0.78
5	1.60	66	0.87
5	4.00	64	0.92
5	10.00	55	0.94
5	25.00	47	0.95
0	0.64	81	0.79
0	1.60	80	0.83
0	4.00	76	0.88
0	10.00	63	0.90
0	25.00	54	0.92

Table A.2: Similar data to Table 5.1 but for solar-mass stars ($0.5\,\mathrm{M_\odot}$ to $2\,\mathrm{M_\odot}$). Percentages of found cluster stars relative to simulated cluster stars and cluster membership attribution reliability score of those findings in the solar-mass range.

Angle °	Mass $\mathrm{kM}_\odot$	% Found	F1 Score
180	0.64	47	0.70
180	1.60	71	0.94
180	4.00	61	0.91
180	10.00	50	0.93
180	25.00	48	0.95
25	0.64	73	0.90
25	1.60	72	0.92
25	4.00	61	0.93
25	10.00	57	0.95
25	25.00	52	0.96
10	0.64	54	0.74
10	1.60	78	0.94
10	4.00	75	0.95
10	10.00	62	0.96
10	25.00	54	0.97
5	0.64	68	0.84
5	1.60	71	0.91
5	4.00	76	0.94
5	10.00	62	0.96
5	25.00	56	0.97
0	0.64	78	0.93
0	1.60	78	0.96
0	4.00	77	0.95
0	10.00	66	0.96
0	25.00	57	0.97

Table A.3: Similar data to Table 5.1 but for high-mass stars ($>2\,\mathrm{M}_\odot$). Percentages of found cluster stars relative to simulated cluster stars and cluster membership attribution reliability score of those findings in the high-mass range.

Bibliography

[1] S. J. Aarseth, M. Henon, and R. Wielen. A Comparison of Numerical Methods for the Study of Star Cluster Dynamics. , 37(1):183–187, December 1974.

[2] Anisa Bajkova and Vadim Bobylev. Parameters of six selected galactic potential models. *Open Astronomy*, 26(1):72–79, 2017.

[3] Barros, D. A., Lépine, J. R. D., and Dias, W. S. Models for the 3d axisymmetric gravitational potential of the milky way galaxy - a detailed modelling of the galactic disk. *A&A*, 593:A108, 2016.

[4] Nate Bastian, Kevin R. Covey, and Michael R. Meyer. A universal stellar initial mass function? a critical look at variations. *Annual Review of Astronomy and Astrophysics*, 48(1):339–389, Aug 2010.

[5] H. Baumgardt and S. Sollima. The global mass functions of 35 galactic globular clusters – ii. clues on the initial mass function and black hole retention fraction. *Monthly Notices of the Royal Astronomical Society*, 472(1):744–750, Aug 2017.

[6] James Binney. Dynamics for Galactic Archaeology. *New Astron. Rev.*, 57:29–51, 2013.

[7] James Binney, Ortwin Gerhard, and David Spergel. The photometric structure of the inner Galaxy. *Monthly Notices of the Royal Astronomical Society*, 288(2):365–374, 06 1997.

[8] James Binney and Scott Tremaine. *Galactic Dynamics: Second Edition*. Princeton University Press, Princeton, rev - revised, 2 edition, 2011.

[9] Jo Bovy. galpy: A python library for galactic dynamics. *The Astrophysical Journal Supplement Series*, 216(2):29, Feb 2015.

[10] Jo Bovy and Scott Tremaine. ON THE LOCAL DARK MATTER DENSITY. *The Astrophysical Journal*, 756(1):89, aug 2012.

[11] Larry Bradley, Brigitta Sipőcz, Thomas Robitaille, Erik Tollerud, Zé Vinícius, Christoph Deil, Kyle Barbary, Tom J Wilson, Ivo Busko, Axel Donath, Hans Moritz Günther, Mihai Cara, krachyon, Simon Conseil, Azalee Bostroem, Michael Droettboom, E. M. Bray, P. L. Lim, Lars Andersen Bratholm, Geert Barentsen, Matt Craig, Shivangee Rathi, Sergio Pascual, Gabriel Perren, Iskren Y. Georgiev, Miguel de Val-Borro, Wolfgang Kerzendorf, Yoonsoo P. Bach, Bruno Quint, and Harrison Souchereau. astropy/photutils: 1.2.0, September 2021.

[12] Wilhelm Busch. *Humoristischer Hausschatz*. Bassermann, München, 5. aufl. edition, 1893.

[13] Bradley W. Carroll and Dale A. Ostlie. *An Introduction to Modern Astrophysics*. Pearson Addison-Wesley, 2nd (international) edition, 2007.

[14] Gilles Chabrier. Galactic Stellar and Substellar Initial Mass Function. , 115(809):763–795, July 2003.

[15] Ryan R. Curtin, Marcus Edel, Mikhail Lozhnikov, Yannis Mentekidis, Sumedh Ghaisas, and Shangtong Zhang. mlpack 3: a fast, flexible machine learning library. *Journal of Open Source Software*, 3(26):726, 2018.

[16] T. de Zeeuw, R. Tamai, and J. Liske. Constructing the E-ELT. *The Messenger*, 158:3–6, December 2014.

[17] Luc Devroye. *Non-Uniform Random Variate Generation(originally published with*. Springer-Verlag, 1986.

[18] Rebecca A. W. Elson, S. Michael Fall, and Kenneth C. Freeman. The Structure of Young Star Clusters in the Large Magellanic Cloud. , 323:54, December 1987.

[19] Espinoza, P., Selman, F. J., and Melnick, J. The massive star initial mass function of the arches cluster ***. *A&A*, 501(2):563–583, 2009.

[20] Martin Ester, Hans-Peter Kriegel, Jörg Sander, and Xiaowei Xu. A density-based algorithm for discovering clusters in large spatial databases with noise. In *Proceedings of the Second International Conference on Knowledge Discovery and Data Mining*, KDD'96, page 226–231. AAAI Press, 1996.

[21] R.P. Feynman, R.B. Leighton, M. Sands, and EM Hafner. *The Feynman Lectures on Physics; Vol. I*, volume 33. AAPT, 1965.

[22] M. et al Galassi. Gnu scientific library reference manual, 2018.

[23] James E. Gentle. *Matrix Algebra: Theory, Computations, and Applications in Statistics*. Springer Publishing Company, Incorporated, 1st edition, 2007.

[24] Oscar A. Gonzalez and Dimitri Gadotti. The milky way bulge: Observed properties and a comparison to external galaxies. *Galactic Bulges*, page 199–232, 2016.

[25] Sanghamitra Goswami, Stefan Umbreit, Matt Bierbaum, and Frederic A. Rasio. Formation of Massive Black Holes in Dense Star Clusters. II. Initial Mass Function and Primordial Mass Segregation. , 752(1):43, June 2012.

[26] Michael Y Grudić, Dávid Guszejnov, Philip F Hopkins, Astrid Lamberts, Michael Boylan-Kolchin, Norman Murray, and Denise Schmitz. From the top down and back up again: star cluster structure from hierarchical star formation. *Monthly Notices of the Royal Astronomical Society*, 481(1):688–702, 08 2018.

[27] S. Harfst, S. Portegies Zwart, and A. Stolte. Reconstructing the arches cluster - i. constraining the initial conditions. *Monthly Notices of the Royal Astronomical Society*, 409(2):628–638, Sep 2010.

[28] Lars Hernquist. An Analytical Model for Spherical Galaxies and Bulges. , 356:359, June 1990.

[29] Lars Hernquist. N-Body Realizations of Compound Galaxies. , 86:389, June 1993.

[30] Ivan R. King. Density Data and Emission Measure for a Model of the Coma Cluster. , 174:L123, June 1972.

[31] Pavel Kroupa. On the variation of the initial mass function. *Monthly Notices of the Royal Astronomical Society*, 322(2):231–246, 04 2001.

[32] Pavel Kroupa. The initial mass function and its variation. *ASP Conf. Ser.*, 285:86, 2002.

[33] Pavel Kroupa and Carsten Weidner. Galactic-field initial mass functions of massive stars. *The Astrophysical Journal*, 598(2):1076–1078, dec 2003.

[34] A. H. W. Kuepper, Th. Maschberger, P. Kroupa, and H. Baumgardt. McLuster: A Tool to Make a Star Cluster, July 2011.

[35] Andrea Kunder, Andreas Koch, R. Michael Rich, Roberto de Propris, Christian D. Howard, Scott A. Stubbs, Christian I. Johnson, Juntai Shen, Yougang Wang, Annie C. Robin, John Kormendy, Mario Soto, Peter Frinchaboy, David B. Reitzel, HongSheng Zhao, and Livia Origlia. THE BULGE RADIAL VELOCITY ASSAY (BRAVA). II. COMPLETE SAMPLE AND DATA RELEASE. *The Astronomical Journal*, 143(3):57, feb 2012.

[36] Byung-Uk Lee. *Stereo Matching of Skull Landmarks*. PhD thesis, Stanford University, Stanford, CA, USA, 1991.

[37] Kieran Leschinski, Hugo Buddelmeijer, Oliver Czoske, Miguel Verdugo, Gijs Verdoes-Kleijn, and Werner W. Zeilinger. Scopesim: a flexible general purpose astronomical instrument data simulation framework in python. *Software and Cyberinfrastructure for Astronomy VI*, Dec 2020.

[38] M. Marks and P. Kroupa. Inverse dynamical population synthesis. *Astronomy Astrophysics*, 543:A8, Jun 2012.

[39] D. J. Marshall, A. C. Robin, C. Reylé, M. Schultheis, and S. Picaud. Modelling the galactic interstellar extinction distribution in three dimensions. *Astronomy Astrophysics*, 453(2):635–651, Jun 2006.

[40] Paul J. McMillan. GalPot: Galaxy potential code, November 2016.

[41] Paul J. McMillan. The mass distribution and gravitational potential of the milky way. *Monthly Notices of the Royal Astronomical Society*, 465(1):76–94, Oct 2016.

[42] M. Miyamoto and R. Nagai. Three-dimensional models for the distribution of mass in galaxies. , 27:533–543, January 1975.

[43] Julio F. Navarro, Carlos S. Frenk, and Simon D. M. White. The structure of cold dark matter halos. *The Astrophysical Journal*, 462:563, May 1996.

[44] Sotirios E. Notaris. Gauss-kronrod quadrature formulae - a survey of fifty years of research. *Electron. Trans. Numer. Anal.*, 45:371–404, 01 2016.

[45] Mark J. Pecaut and Eric E. Mamajek. Intrinsic Colors, Temperatures, and Bolometric Corrections of Pre-main-sequence Stars. , 208(1):9, September 2013.

[46] A. J. Pickles. A Stellar Spectral Flux Library: 1150-25000 Å. , 110(749):863–878, July 1998.

[47] R. Piessens, E. de Doncker-Kapenga, and C. W. Ueberhuber. *Quadpack : a subroutine package for automatic integration*. Springer series in computational mathematics ; 1. Springer, Berlin [u.a.], 1983.

[48] H. C. Plummer. On the problem of distribution in globular star clusters. , 71:460–470, March 1911.

[49] Alicia Porras, I. Cruz-González, and Luis Salas. Imf in perseus arm yscs. *ASP Conference Series*, 287:98–103, 01 2003.

[50] Simon F. Portegies Zwart, Stephen L.W. McMillan, and Mark Gieles. Young massive star clusters. *Annual Review of Astronomy and Astrophysics*, 48(1):431–493, Aug 2010.

[51] L. Portinari. The Role of the IMF in Modelling Clusters of Galaxies. In A. Vallenari, R. Tantalo, L. Portinari, and A. Moretti, editors, *From Stars to Galaxies: Building the Pieces to Build Up the Universe*, volume 374 of *Astronomical Society of the Pacific Conference Series*, page 131, December 2007.

[52] Adrian M. Price-Whelan, David W. Hogg, Kathryn V. Johnston, and David Hendel. Inferring the gravitational potential of the milky way with a few precisely measured stars. *The Astrophysical Journal*, 794(1):4, Sep 2014.

[53] A. C. Robin, D. J. Marshall, M. Schultheis, and C. Reylé. Stellar populations in the milky way bulge region: towards solving the galactic bulge and bar shapes using 2mass data. *Astronomy Astrophysics*, 538:A106, Feb 2012.

[54] Edwin E. Salpeter. The Luminosity Function and Stellar Evolution. , 121:161, January 1955.

[55] A. Saro, S. Borgani, L. Tornatore, K. Dolag, G. Murante, A. Biviano, F. Calura, and S. Charlot. Properties of the galaxy population in hydrodynamical simulations of clusters. *Monthly Notices of the Royal Astronomical Society*, 373(1):397–410, Nov 2006.

[56] Ralph Schönrich, James Binney, and Walter Dehnen. Local kinematics and the local standard of rest. , 403(4):1829–1833, April 2010.

[57] P. Kenneth. Seidelmann, Great Britain., and United States Naval Observatory. *Explanatory supplement to the astronomical almanac / prepared by the Nautical Almanac Office, U.S. Naval Observatory ; with contributions from H.M. Nautical Alamanac Office, Royal Greenwich Observatory ... [et al.] ; edited by P. Kenneth Seidelmann*. University Science Books Mill Valley, Calif, [rev. ed.]. edition, 1992.

[58] A. Toomre. On the gravitational stability of a disk of stars. , 139:1217–1238, May 1964.

[59] P. C. van der Kruit. The three-dimensional distribution of light and mass in disks of spiral galaxies. , 192:117–127, March 1988.

[60] P. C. van der Kruit and L. Searle. Surface photometry of edge-on spiral galaxies. I - A model for the three-dimensional distribution of light in galactic disks. , 95:105–115, February 1981.

[61] John Vince. *Mathematics for Computer Graphics*. Springer, 01 2006.

[62] D. L. Walker, S. N. Longmore, N. Bastian, J. M. D. Kruijssen, J. M. Rathborne, R. Galván-Madrid, and H. B. Liu. Comparing young massive clusters and their progenitor clouds in the Milky Way. *Monthly Notices of the Royal Astronomical Society*, 457(4):4536–4545, 02 2016.

[63] Yougang Wang, Hongsheng Zhao, Shude Mao, and R. M. Rich. A new model for the Milky Way bar. *Monthly Notices of the Royal Astronomical Society*, 427(2):1429–1440, 12 2012.

[64] Denis Yurin and Volker Springel. An iterative method for the construction of N-body galaxy models in collisionless equilibrium. *Monthly Notices of the Royal Astronomical Society*, 444(1):62–79, 08 2014.

Acronyms

BPL Broken Power Law 16, 18

CBE collisionless Boltzmann Equation 27

CDF cumulative distribution function 13

COM centre of mass 15

COV cone of vision 22, 23, 34, 35

CS cluster star 9, 34, 36, 44, 46–48, 50, 51

ELT Extremely Large Telescope 2, 3, 11, 12, 34, 36, 44, 56

FN False Negative 49–51

FOV field of view 12, 34, 35

FP False Positive 49–51

FS field star 9, 10, 12, 14, 18, 20, 22, 25, 29, 34–36, 44, 46–48, 50, 51, 55

GC Galactic Centre 2, 8, 9, 11, 19, 34, 35, 37, 42, 44–49, 51, 55, 56

GSL GNU Scientific Library 13, 20

HTP Heliocentric Telescope Polar 9, 10, 40–42, 44, 45, 51, 55

IMF Initial Mass Function 2, 3, 8, 11, 12, 15–18, 46, 50, 51, 56

MCS mapped cluster star 51

MFS mapped field star 51

MS mapped star 51

MW Milky Way 18, 19, 29, 31, 56

NCDF normalized cumulative distribution function 16–18

NFW Navarro–Frenk–White 18

OS observed star 51

PDF probability density function 12

PDMF present day mass function 8, 16, 24, 25

PSF point spread function 41, 42, 49

SCS simulated cluster star 51

SFS simulated field star 51

SS simulated star 51

TN True Negative 49, 51

TP True Positive 49, 50

UN Unconfirmed Negative 49

UP Unconfirmed Positive 49, 50

YMC Young Massive Cluster 11, 18, 56